Original Article

Molecular and immune characterization of Chinese early-stage non-squamous non-small cell lung cancer: a multi-omics cohort study

Haoxin Peng[1,2,3#], Xiangrong Wu[2,3,4#], Xiaoli Cui[5#], Shaopeng Liu[6,7#], Yueting Liang[8#], Xiuyu Cai[9], Mengping Shi[6], Ran Zhong[2], Caichen Li[2], Jun Liu[2], Dongfang Wu[5], Zhibo Gao[5], Xu Lu[6,7], Haitao Luo[5], Jianxing He[2], Wenhua Liang[2,10]

[1]Department of Gastrointestinal Oncology, Key Laboratory of Carcinogenesis and Translational Research (Ministry of Education), Peking University Cancer Hospital & Institute, Beijing, China; [2]Department of Thoracic Oncology and Surgery, China State Key Laboratory of Respiratory Disease & National Clinical Research Center for Respiratory Disease, the First Affiliated Hospital of Guangzhou Medical University, Guangzhou, China; [3]Department of Clinical Medicine, Nanshan School, Guangzhou Medical University, Guangzhou, China; [4]Department of Oncology, Shanghai Medical College, Fudan University, Shanghai, China; [5]Shenzhen Engineering Center for Translational Medicine of Precision Cancer Immunodiagnosis and Therapy, YuceBio Technology Co., Ltd., Shenzhen, China; [6]Department of Computer Science, Guangdong Polytechnic Normal University, Guangzhou, China; [7]Department of Artificial Intelligence Research, Pazhou Lab, Guangzhou, China; [8]Department of Radiation Oncology, Peking University Cancer Hospital & Institute, Beijing, China; [9]Department of General Internal Medicine, Sun Yat-sen University Cancer Center, State Key Laboratory of Oncology in South China, Collaborative Innovation Cener for Cancer Medicine, Guangzhou, China; [10]Department of Medical Oncology, The First People's Hospital of Zhaoqing, Zhaoqing, China

Contributions: (I) Conception and design: H Peng, X Wu, W Liang; (II) Administrative support: W Liang, J He; (III) Provision of study materials or patients: All authors; (IV) Collection and assembly of data: H Peng, X Wu, W Liang; (V) Data analysis and interpretation: H Peng, X Wu, S Liu, W Liang; (VI) Manuscript writing: All authors; (VII) Final approval of manuscript: All authors.

[#]These authors contributed equally to this work.

Correspondence to: Haitao Luo, PhD. Shenzhen Engineering Center for Translational Medicine of Precision Cancer Immunodiagnosis and Therapy, YuceBio Technology Co., Ltd., Shenyan Road, Yantian District, Shenzhen 518000, China. Email: luohaitao@yucebio.com; Jianxing He, MD, PhD, FACS, FRCS, AATS active member, ESTS member. Department of Thoracic Oncology and Surgery, China State Key Laboratory of Respiratory Disease & National Clinical Research Center for Respiratory Disease, the First Affiliated Hospital of Guangzhou Medical University, Yanjiang West Road, Yuexiu District, Guangzhou 510000, China. Email: drjianxing.he@gmail.com; Wenhua Liang, MD. Department of Thoracic Oncology and Surgery, China State Key Laboratory of Respiratory Disease & National Clinical Research Center for Respiratory Disease, the First Affiliated Hospital of Guangzhou Medical University, Yanjiang West Road, Yuexiu District, Guangzhou 510000, China; Department of Medical Oncology, The First People's Hospital of Zhaoqing, Donggang East Road, Duanzhou District, Zhaoqing 526000, China. Email: liangwh1987@163.com.

Background: Albeit considered with superior survival, around 30% of the early-stage non-squamous non-small cell lung cancer (Ns-NSCLC) patients relapse within 5 years, suggesting unique biology. However, the biological characteristics of early-stage Ns-NSCLC, especially in the Chinese population, are still unclear.

Methods: Multi-omics interrogation of early-stage Ns-NSCLC (stage I–III), paired blood samples and normal lung tissues (n=76) by whole-exome sequencing (WES), RNA sequencing, and T-cell receptor (TCR) sequencing were conducted.

Results: An average of 128 exonic mutations were identified, and the most frequently mutant gene was *EGFR* (55%), followed by *TP53* (37%) and *TTN* (26%). Mutations in *MUC17*, *ABCA2*, *PDE4DIP*, and *MYO18B* predicted significantly unfavorable disease-free survival (DFS). Moreover, cytobands amplifications in 8q24.3, 14q13.1, 14q11.2, and deletion in 3p21.1 were highlighted in recurrent cases. Higher incidence of human leukocyte antigen loss of heterozygosity (HLA-LOH), higher tumor mutational burden (TMB) and tumor neoantigen burden (TNB) were identified in ever-smokers than never-smokers. HLA-LOH also correlated with higher TMB, TNB, intratumoral heterogeneity (ITH), and whole chromosomal instability (wCIN) scores. Interestingly, higher ITH was an independent predictor of better DFS in early-stage Ns-NSCLC. Up-regulation of immune-related genes, including *CRABP2*, *ULBP2*, *IL31RA*, and *IL1A*,

independently portended a dismal prognosis. Enhanced TCR diversity of peripheral blood mononuclear cells (PBMCs) predicted better prognosis, indicative of a noninvasive method for relapse surveillance. Eventually, seven machine-learning (ML) algorithms were employed to evaluate the predictive accuracy of clinical, genomic, transcriptomic, and TCR repertoire data on DFS, showing that clinical and RNA features combination in the random forest (RF) algorithm, with area under the curve (AUC) of 97.5% and 83.3% in the training and testing cohort, respectively, significantly outperformed other methods.

Conclusions: This study comprehensively profiled the genomic, transcriptomic, and TCR repertoire spectrums of Chinese early-stage Ns-NSCLC, shedding light on biological underpinnings and candidate biomarkers for prognosis development.

Keywords: Early-stage lung cancer (early-stage LC); multi-omics; machine-learning (ML); disease-free survival (DFS)

Submitted Dec 02, 2023. Accepted for publication Mar 15, 2024. Published online Apr 25, 2024.
doi: 10.21037/tlcr-23-800
View this article at: https://dx.doi.org/10.21037/tlcr-23-800

Introduction

Lung cancer (LC) is among the most diagnosed cancers and the predominant cause of cancer-related death globally (1). Despite a dramatic improvement in LC prognoses with the advent of targeted therapies, especially in lung adenocarcinoma (LUAD), more advances are restricted by the poor comprehension of its pathogenesis (2). Non-small cell lung cancer (NSCLC) is the major subtype of LC, and a remarkable increase in detecting early-stage non-squamous NSCLC (Ns-NSCLC) was observed with the growing application of low-dose computed tomography screening (3,4). While radical resection is the primary treatment option for early-stage Ns-NSCLC, around 30% of the patients die of relapse within 5 years (5). Therefore, it is essential to comprehensively characterize the early-stage Ns-NSCLC by multi-dimension approaches, including genomic, transcriptomic, proteomic, and immunological profiling, which may help risk stratification and personalized strategy development.

Diverse gene mutations, fusions, copy number variations (CNVs), and epigenetic variations have been depicted with the development of the next-generation sequencing (NGS) technique, accentuating the intratumoral and intertumoral heterogeneity of NSCLC (6,7). For instance, *KRAS* and *EGFR* mutations are commonly detected in smoker and non-smoker LUAD, respectively (8). Meanwhile, mutations in *TP53* and *PIK3CA* are most frequently identified in lung squamous cell cancer (LUSC) (9). Moreover, Kadara and colleagues reported that mutation in *SETD2* correlated with poor prognosis, and *EGFR* and *PIK3CA* mutations predicted unfavorable responses to adjuvant chemotherapy of early-stage LUAD in the American population (10). Choi *et al.* further found that *MLL2* mutation correlated with unfavorable recurrence-free survival of American early-stage LUSC patients (11). Although these variations have been

Highlight box

Key findings

- This study comprehensively profiled the genomic, transcriptomic, and T-cell receptor repertoire spectrums of Chinese early-stage non-squamous non-small cell lung cancer (Ns-NSCLC), which may affect prognosis and influence the crosstalk between tumor and the immune system, unveiling novel cancer biological meanings.

What is known and what is new?

- Several molecular and immune characteristics of non-small cell lung cancer (NSCLC) have been identified previously, while their associations with prognoses were unclear.
- We innovatively characterized the multi-omics features of Chinese early-stage Ns-NSCLC and interrogated the relationships between various alterations, either alone or in combination, with prognosis. A robust multi-omics prognostic model was also established, demonstrating the best performer in integrating clinical and molecular features.

What is the implication, and what should change now?

- The reported biological underpinnings and candidate biomarkers of Chinese Ns-NSCLC may contribute to therapy and prognosis development.
- Prospective and cross-cohort validation examining the associations or causalities between the findings and clinical outcomes are requisite for better clinical practice.

implicated in the classical cancer signal pathways and have deepened our knowledge of the molecular pathogenesis of NSCLC, their associations with prognoses and personalized therapeutic strategies in early-stage NSCLC, especially in the Chinese population, are still unclear.

At the transcriptomic level, a previous study has classified three predominant LUAD subtypes, including the terminal respiratory unit, proximal proliferative and proximal inflammatory subcluster, indicative of the potential for precise treatment (12). Other groups have also established gene expression-based models, like immune-related gene signature, to predict prognosis and treatment response (13,14), underscoring the important role of the immune microenvironment in LC pathobiology.

The essential role of the immune components in the tumor microenvironment (TME) is also accentuated by recent successes describing durable responses to immune checkpoint inhibitors (ICIs) of NSCLC patients (15). The biological underpinnings of successful immunotherapy are precisely recognizing neoantigen peptides by clonally proliferative T-cell receptors (TCRs) and subsequent activation of tumoricidal effects by the host immune system (16). TCR repertoire represents the strength and breadth of T-cell response, undertaking a vital role in antitumor immunity across various cancers (17). Recent studies have demonstrated the predictive and prognostic roles of peripheral TCR repertoire in ICIs therapies of advanced NSCLC (18,19). Nonetheless, the TCR repertoire landscape concerning different genetic alterations and its prognostic significance of early-stage Ns-NSCLC remains to be uncovered.

In the present study, we comprehensively profiled the genomic, transcriptomic, and TCR repertoire spectrums of Chinese early-stage Ns-NSCLC, accentuating the unique biological heterogeneity and biomolecular network. Rich annotation of this cohort also enabled us to interrogate the relationships between various alterations, either alone or in combination, with prognosis. Eventually, a robust multi-omics prognostic model was established, demonstrating the best performer integrating clinical and molecular features. We present this article in accordance with the TRIPOD reporting checklist (available at https://tlcr.amegroups.com/article/view/10.21037/tlcr-23-800/rc).

Methods

Study population and sample collection

Radically resected Ns-NSCLC, matched blood samples, and normal lung tissues (n=76 pairs) were collected at the First Affiliated Hospital of Guangzhou Medical University (GZMU1H) between 2012 and 2015. Eligible patients were stage IA–III pathologically confirmed Ns-NSCLC and no personal history of cancer (20). Patients who (I) underwent neoadjuvant therapy; (II) did not have R0 excision; and (III) had multiple primary LCs were excluded. Informed consent of included patients was obtained, and this research was approved by the GZMU1H Ethics Committee (approval No. KLS-17-03). The study was conducted in accordance with the Declaration of Helsinki (as revised in 2013) (21).

Multi-omics detection of the samples was completed at Yucebio Technology Co., Ltd. (Shenzhen, China). Details of the kits and software used are available in Tables S1,S2.

Processing whole-exome sequencing (WES) data

Library preparation and sequencing

We extracted genomic DNAs from formalin-fixed paraffin-embedded (FFPE) slides and the matched blood controls (BCs) by QIAamp DNA FFPE Tissue Kit and DNeasy Blood and Tissue Kit (Qiagen, USA), respectively, which were subsequently quantified by Qubit 3.0 via the dsDNA HS Assay Kit (ThermoFisher Scientific, USA). Library preparations were conducted by KAPA Hyper Prep Kit (KAPA Biosystems, USA). Target enrichment was performed by the xGen Exome Research Panel and Hybridization and Wash Reagents Kit (Integrated DNA Technologies, USA). Sequencing was carried out on the Illumina HiSeq4000 platform (Illumina, USA), and the average sequencing depths were 140× and 64× for tumors and normal BCs, respectively.

Data processing of exome libraries

We filtered out the N rate beyond 10% and low-quality reads by SOAPnuke. The Burrows-Wheeler Alignment tool was utilized to align the clean reads to the human reference genome based on the UCSC hg19. Conversing, sorting, and indexing alignment data was performed via SAMtools. SAMBLASTER was used to mark the duplicates for decreasing biases.

Copy number variants and intratumoral heterogeneity (ITH) analyses

The VarScan software was employed to identify somatic mutations, including small insertions and deletions (indels) and single nucleotide variants. Aiming at retrieving false-negative mutations and removing false-positive mutations,

strict selection was conducted by our in-house variant detection tool. Subsequently, each mutation was annotated by the SnpEff software. CNVs were determined by exome-wide profile comparisons between tumors and matched BCs via CNVkit. The cancer cell fraction of mutations was calculated by PyClone, with the tumor purity computed by All-FIT. The proportions of subclone mutations to all mutations were defined as ITH (22).

Human leukocyte antigen (HLA) typing and loss of heterozygosity (LOH) analysis

HLA typing of the paired tumor and BCs was estimated from WES data via POLYSOLVER and Bwakit software. Then LOH in the HLA approach was employed, and LOH was determined if (I) a copy number <0.5 and (II) imbalanced allelic identified by P<0.01 by the paired Student's *t*-test between the two distributions (23).

Genomic biomarker analyses

Tumor mutational burden (TMB) was defined as the number of non-synonymous somatic mutations per mega-base (Mb) of the genome interrogated. Through in-house software centering on mutant amino acids, all indels and non-synonymous mutations were translated into 21-mer peptide sequences, which were subsequently utilized to create a 9- to 11-mer peptide by the sliding window method for predicting major histocompatibility complex (MHC) class I binding affinity. The NetMHCpan software was employed for predicting the binding intensity of mutant peptides to patient-specific HLA alleles. The estimated binding strength of a peptide with any HLA allele was selected if half-maximal inhibitory concentration (IC50) <500 nM. Consequently, neoantigen was calculated as multifarious selective peptides generated from the same mutation. Tumor neoantigen burden (TNB) was determined by the number of such peptides per Mb of the genome interrogated. The whole chromosomal instability (wCIN) score was utilized to assess the copy number burden by the allele-specific copy number analysis of tumors (ASCAT) approach (24). Gene mutation pathway analyses were conducted as previously described (25).

RNA sequencing workflow

We isolated the total RNA of tumor samples from the tumor tissues via RNeasy Plus Universal Kit (Qiagen, USA). Utilizing the Qubit™ RNA HS Assay Kit, the concentrations of the extracted RNA were then quantified. The integrity and purity of the extracted RNA were tested by the RNA Cartridge kit of the Qseq100 Bio-Fragment Analyzer (Bioptic, China) and the Take3 kits (BioTek, USA), respectively. We then generated the RNA-seq libraries by the VAHTS mRNA-seq V3 Library Prep Kit (Vazyme, China). Eventually, the libraries were sequenced on the NextSeq 550AR (Illumina, USA) with 150-bp paired-end reads.

Gene expression analysis

Low-quality adapters and reads from raw RNA sequencing data were filtered by trim galore. The read counts and transcripts per million values were analyzed via Kallisto based on the Gencode database (26). Identification of differentially expressed genes (DEGs) was conducted based on the read counts matrix, of which DEGs with P value <0.05 and $|\log_2 \text{foldchange}| > 1$ were considered significant. Gene set enrichment and variation analysis based on Gene Ontology and Kyoto Encyclopedia of Genes and Genomes datasets were utilized to interrogate the pathway activity differences between groups (27). Enriched pathways with Bonferroni-corrected $P_{adj}<0.05$ were considered significant (28).

TCR sequencing

Isolating from peripheral blood mononuclear cells (PBMCs) by RNeasy Plus Mini Kit, the concentration of total RNA was detected by the Take3 kit. Via iRepertoire Short Read iR-Profile Reagent System HTBI-vc (iRepertoire, USA), total RNA was synthesized into the cDNA library. Sequencing was conducted on the NextSeq 550AR system with 150-bp paired-end reads. We then trimmed Fastq reads concerning their low-quality 3' ends bases. Integration of processed pair-end reads was executed based on overlapped alignment with the adjusted Needleman-Wunsch method. Identification of the CDR3 sequences of V-D-J gene fragments with reference sequences from the IMGT database (29) was conducted on the MiXCR (30). Evaluation of the immune repertoire sequencing was carried out on the VDJtools (31). Additionally, we executed frequency-based adjustments on samples. The chaoE, shannonWiener, Simpson, and d50 indexes were utilized to assess the TCR clone diversity.

Estimation of cellular abundance by bulk RNA-seq data

CIBERSORT, an approach assessing the contents of 22 kinds of immune cell populations, including natural killer (NK) cell, B cell, T cell, dendritic cell (DC), monocyte, macrophage, mast cell, neutrophil, eosinophil, and their

subclusters, was used to uncover the immune infiltrating spectrums by bulk RNA-seq data (32). MCP-counter, a versatile computational approach which robustly quantifies the absolute abundance of two stromal and eight immune cell populations from bulk transcriptomic data, was also exploited (33).

Construction and validation of the multi-omics prognostic model

The multi-omics prognostic model was constructed and validated according to the TRIPOD checklist (34). The machine-learning (ML) framework was built on Python (version 3.9.13) using the following libraries: scikit-learn (version 1.2.2), pandas (version 1.5.3), scipy (version 1.9.1), and imbalanced-learn (version 0.10.1).

We performed combinations of different omics biomarkers: (I) Clinical features + DNA; (II) Clinical features + RNA; (III) Clinical features + TCR; (IV) Clinical features + DNA + RNA; (V) Clinical features + DNA + RNA + TCR; (VI) DNA + RNA; (VII) DNA + RNA + TCR, resulting in seven different datasets. Seven ML approaches, including decision tree classifier (DTC), extra tree classifier (ETC), gradient boosting classifier (GBC), Gaussian process classifier (GPC), K-nearest neighbors (KNN), random forest (RF), and support vector machine (SVM) were adopted to screen out the robust prognosticators and develop the multi-omics prognostic model.

Each dataset (n=76) was divided into a training cohort (n=60, 80%) and an internal testing cohort (n=16, 20%) via stratified sampling (35). For the data input to the KNN model, we used Z-score normalization to scale the original data and transform it into a standard normal distribution. This process eliminated dimensionality differences between features, balancing the impact of various features on the model. For the data input to the GPC model, we applied the Synthetic Minority Over-sampling Technique (SMOTE) preprocessing method. SMOTE approach generates synthetic samples by computing the differences between minority class samples and their nearest neighbors, achieving a balance of sample categories in the dataset. The remaining models were trained via the original and unprocessed data.

Grid search and five-fold cross-validation were employed to perform hyperparameter optimization and model performance evaluation on five algorithms except for KNN and GPC. Specifically, the grid search method exhaustively searched all possible combinations within a given parameter space. Table S3 provides detailed information on hyperparameter combinations per model. In five-fold cross-validation, we divided the training set into five equal-sized subsets. We selected four subsets as the training set and the remaining one subset as the validation set. By performing this process five times, with a different subset as the validation set per trial, we obtained five sets of training results. We compared the performance of each parameter combination on training metrics to determine the best parameter combination, optimizing model performance and preventing overfitting. Accuracy (ACC) and area under the curve (AUC) are the major metrics to measure the performance of the models. Other evaluation indices like precision, recall, and F1-score were also employed.

After training on all datasets, we selected the more accurate and stabler tree-based algorithms: RF and ETC. Gini importance analysis was subsequently used to assess the importance of specific features within each dataset. The Gini index measured the purity or impurity of samples within a node. In binary classification issues, the calculation formula for the Gini index is given by $\text{Gini index} = 1 - \left(p_1^2 + p_2^2 \right)$, where p_1 and p_2 represents the proportions of samples belonging to two different classes within the node. Gini importance measures the importance of a feature by calculating the reduction in the average Gini index for each feature over all nodes of the decision tree. Given that RF and ETC are both ensemble methods of decision trees, we aggregated the Gini importance of each corresponding feature across all trees, resulting in the final Gini index.

External dataset utilized for analyses

The genomic profiles, mRNA expression, and clinical characteristics data of LUAD samples from The Cancer Genome Atlas (TCGA)-LUAD cohort were downloaded from the UCSC Xena (https://xena.ucsc.edu/) database (acquisition date, 2023/1/11).

Statistical analysis

The Mann-Whitney *U* test, Wilcoxon *t*-test, and Kruskal-Wallis test were employed to compare the differences of continuous and categorical data. Spearman rank correlation test was used to evaluate the correlation between two variables, and the |correlation coefficient| >0.5 was regarded as significant. Survival differences between two groups were evaluated by the Kaplan-Meier approach and the log-rank test. Univariate and multivariate Cox regression analyses correcting for age, sex, and clinical tumor staging (cTNM)

Table 1 Baseline characteristics of the included patients

Characteristics	Disease-free		Relapse		P value
	Number	Percentage (%)	Number	Percentage (%)	
Gender					0.23
Female	27	54	10	38.46	
Male	23	46	16	61.54	
Smoking status					0.45
Never	33	66	17	65.38	
Former	10	20	3	11.54	
Current	7	14	6	23.08	
Stage					0.003
IA	16	32	3	11.54	
IB	15	30	4	15.38	
II	12	24	6	23.08	
III	7	14	13	50	
EGFR					0.09
Mutant	24	48	18	69.23	
Wild-type	26	52	8	30.77	

were utilized to assess the prognostic effect of signature. The X-tile software was employed to determine the optimal cutoff point of continuous variables (36). The receiver operating characteristic (ROC) curves and the corresponding predictive ACC were analyzed via the AUC values. DeLong's test was utilized to compare the predictivity ACC, evaluated by AUCs, between different methods. Statistical analyses and plot generation were performed in GraphPad Prism (version 8.0), SPSS (version 25.0), and R (version 4.0.4). P value <0.05 of statistical analyses was regarded as significant. Data were presented by mean ± standard error or by box and whisker plots.

Results

Baseline characteristics of the included patients

A total of 76 patients, with the majority of LUAD samples (n=68, 89%), meeting the inclusion criteria were recruited (*Table 1*). The median age was 60 (ranging from 36 to 86) years, and 34.2% of the patients were ever-smokers. Twenty-six patients relapsed during the follow-up period, and the recurrent rates of IA, IB, II, and III samples were 11.54%, 15.38%, 23.08%, and 50%, respectively.

Quality control of the multi-omics data

After appropriate sample quality control, a total of 76 paired tumor-control WES data, 71 paired tumor-paratumor RNA-sequencing data, and 139 cases of TCR-sequencing data of tumor-paratumor-blood samples were eligible for downstream analyses (*Figure 1A*).

Molecular profiling of early-stage Ns-NSCLC

The mutation landscape of early-stage Ns-NSCLC was depicted, showing that *EGFR* was the most frequently mutant gene (55%), followed by *TP53* (37%) and *TTN* (26%) (*Figure 1B*), accordant with the recent report (37). A mean of 128 mutations was observed, and ever-smokers harbored significantly more somatic mutations than never-smokers (mean: 238 *vs.* 70, P<0.001), consistent with previous literature (38). The most common base substitutions were C > A and C > T transversions, and they were more frequently detected in ever than never smokers (P<0.01) (*Figure 1C*).

We also compared the mutation landscape between the present and the TCGA-LUAD cohorts (available at https://xena.ucsc.edu/) (Figure S1A). Among the top ten mutant genes in our cohort, the mutation frequencies of *EGFR* (55%

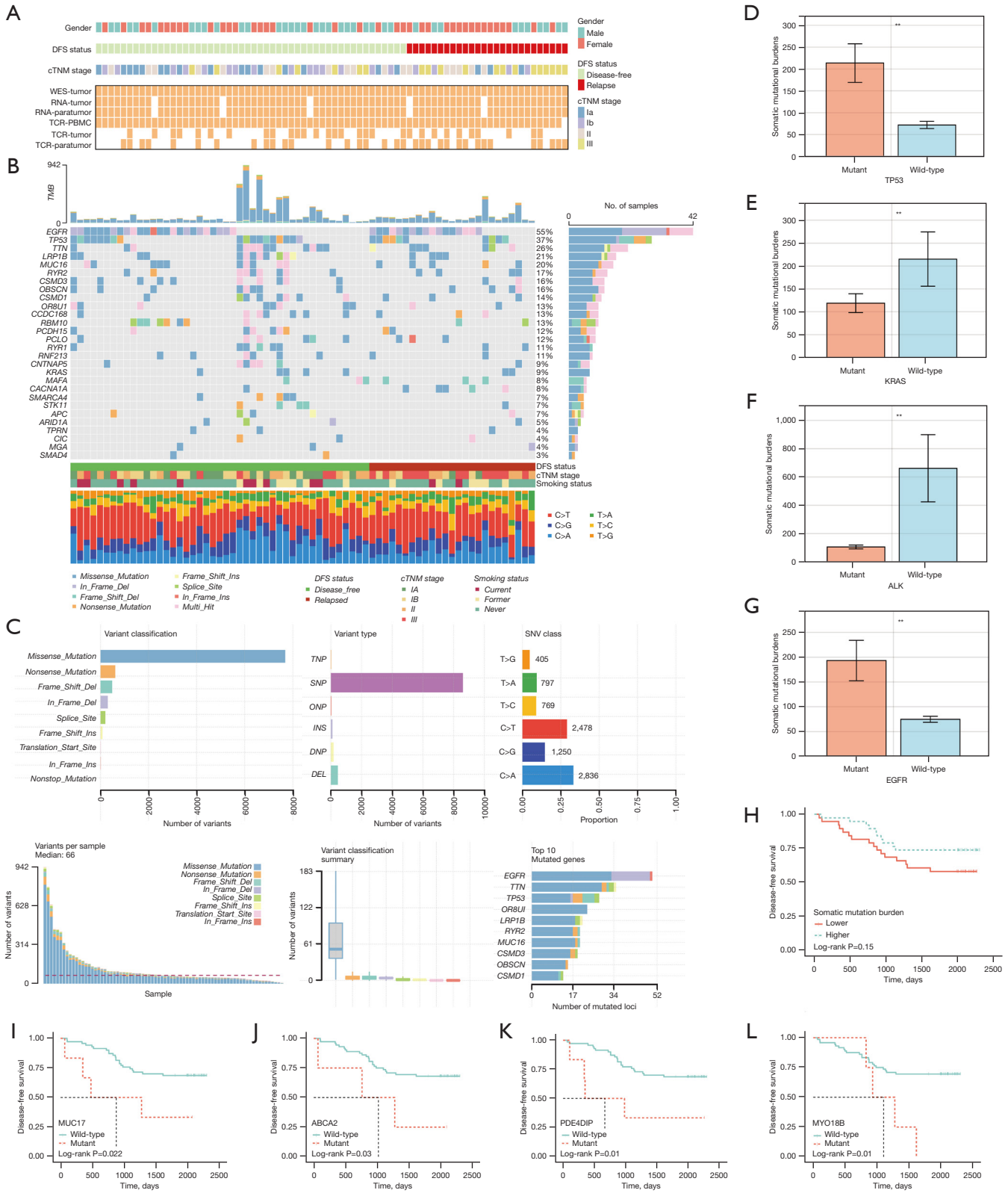

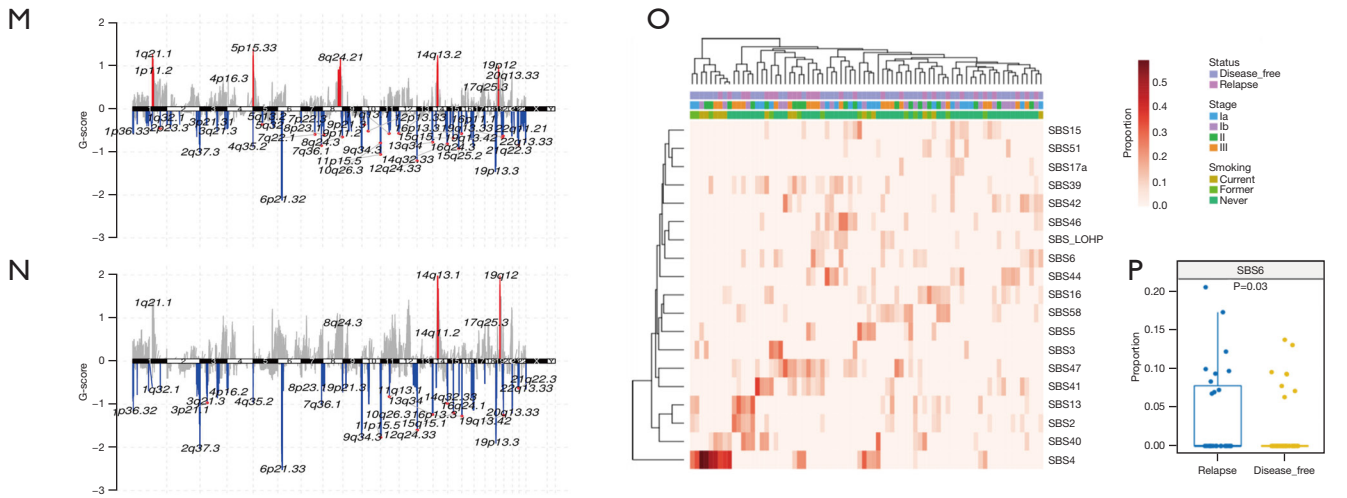

Figure 1 Mutation landscape of Chinese early-stage Ns-NSCLC in the GZMU1H cohort. Paired sample information for multi-omics interrogation (A). Mutation profiles of Chinese early-stage Ns-NSCLC, each column representing an individual patient. The upper barplot demonstrates mutational load, and the right barplot shows the mutation frequency of individual genes (B). Summary of genetic variants, including numbers, classifications, and types (C). Somatic mutational burden differences concerning different driver genes, including *TP53* (D), *KRAS* (E), *ALK* (F), and *EGFR* (G). DFS differences between different levels of somatic mutational burden (H). Monogenic mutation, including *MUC17* (I), *ABCA2* (J), *PDE4DIP* (K), and *MYO18B* (L), showed prognostic significance of DFS. Somatic copy number alteration differences of patients without (M) or with (N) relapse. Single-base substitution signature differences concerning smoking status (O) and relapse status (P). Comparison of continuous data by Wilcoxon *t*-test, **, P<0.01. Data were presented by mean ± standard error for (D-G). Data were presented by box and whisker plots for (C,P). The horizontal bar inside the boxes represents the median, and the lower and upper ends of the boxes are the first and third quartiles. The whiskers indicate values within 1.5× the inter-quartile range from the upper or lower quartile. The dots represent the value of the individual sample. The meanings of the different colors are presented in (C; bottom left) and the colors used are consistent among the top left, bottom left, bottom middle, and bottom right parts of (C). DFS, disease-free survival; cTNM, clinical tumor staging; WES, whole-exome sequencing; TCR, T-cell receptor; PBMC, peripheral blood mononuclear cells; TMB, tumor mutational burden; DEL, delete; TNP, tri-nucleotide polymorphism; SNP, single nucleotide polymorphism; ONP, oligo-nucleotide polymorphism; INS, insert; DNP, di-nucleotide polymorphism; SNV, single nucleotide variation; SBS, single-base substitution; Ns-NSCLC, non-squamous non-small cell lung cancer; GZMU1H, the First Affiliated Hospital of Guangzhou Medical University.

vs. 13%, P<0.001), *TP53* (37% *vs.* 50%, P=0.03), *TTN* (26% *vs.* 48%, P=0.02), *LRP1B* (21% *vs.* 34%, P=0.02), *MUC16* (20% *vs.* 42%, P<0.001), *RYR2* (17% *vs.* 37%, P<0.001), and *CSMD3* (16% *vs.* 40%, P<0.001), were significantly different from Chinese and Caucasian patients (Figure S1B-S1H), underscoring LC genome diversity between ethnicities (38).

Ns-NSCLC with mutant *TP53* (*Figure 1D*), *KRAS* (*Figure 1E*), and *ALK* (*Figure 1F*) displayed higher somatic mutational burden than wild-type ones (P<0.01). On the contrary, the mutation in *EGFR* (*Figure 1G*) predicted lower somatic mutational burden than wild-type ones (P<0.01). Moreover, early-stage Ns-NSCLC harboring higher somatic mutational burden exhibited a trend of better DFS than fewer ones (*Figure 1H*). Higher mutation frequencies of *ASXL1*, *ANK3*, *FGD5*, *FLT4*, *MYO18B*, *MYO3A*, and *SELENOV* were observed in patients with recurrence than without.

Mutations in *MUC17* [hazard ratio (HR) 3.252, 95% confidence interval (CI): 1.118–9.463, P=0.02] (*Figure 1I*), *ABCA2* (HR 3.363, 95% CI: 1.007–11.232, P=0.03) (*Figure 1J*), *PDE4DIP* (HR 3.647, 95% CI: 1.250–10.637, P=0.01) (*Figure 1K*), and *MYO18B* (HR 3.502, 95% CI: 1.201–10.211, P=0.01) (*Figure 1L*) were found to predict significantly shorter disease-free survival (DFS) in the univariate Cox setting. Nonetheless, mutations in these four genes did not correlate with prognosis in the TCGA-LUAD cohort from Caucasian populations, suggesting genomic differences (Figure S2A-S2D). Moreover, the transcriptomic spectrums were significantly different between mutant and wild-type populations. The DEGs of these four genes were

enriched into up-regulation of the cell cycle process and down-regulation of epithelial cell development, representing malignant transformation of cells (Figure S2E-S2L). Intriguingly, the mutation in *MUC17* also correlated with higher neutrophil-mediated immunity of Ns-NSCLC.

As for somatic copy number alteration (sCNA), more frequent deletion (Del) than amplification (*Amp*) genes were observed generally. Significant Dels in 8q24.3, 7q22.1 (containing *COL1A2* gene), and 15q25.2 and Amps in the 4p16.3 (encoding *FGFR3* gene), 5p15.33, and 8q24.21 (encoding *MYC* gene) were found in patients without relapse (*Figure 1M*). Significant Amps in 8q24.3, 14q13.1, and 14q11.2, and Del in 3p21.1 were highlighted in early-stage recurrent Ns-NSCLC (*Figure 1N*). The frequency of smoking-related single-base substitution 4 (SBS4) was the highest among all SBS signatures (*Figure 1O*) (39). Moreover, the frequency of mismatch-repair-deficient-related SBS6 signature was higher in patients with relapse than without (*Figure 1P*) (40).

Landscape of genomic biomarkers and their prognostic effects

The median values of TMB, TNB, and wCIN-score were 2.065 mut/Mb, 0.850 na/Mb, and 0.010, respectively (*Figure 2A*). HLA-LOH was discovered in 28.9% (22 of 76) of Ns-NSCLC patients and was more frequently identified in ever-smokers than never-smokers (P=0.01), consistent with previous findings (23). The incidence of lost alleles was highest in HLA-A (14.5%) and lowest in HLA-C (2.6%).

TMB and TNB were significantly higher in ever-smokers than never-smokers (P<0.001), indicative of a higher mutational burden (*Figure 2B*). Moreover, TP53 mutation was associated with significantly higher TMB, TNB, ITH, and wCIN-score (P<0.05) (*Figure 2C*). Likewise, TTN mutation correlated with higher TMB and TNB (P<0.001), indicative of higher immunogenicity (*Figure 2D*) and has been reported to be a potential predictor of ICIs efficiency (41). Additionally, strong correlations of TMB-TNB (R=0.93, P<0.001) (*Figure 2E*) and TMB-wCIN (R=0.40, P<0.001) (*Figure 2F*) were observed.

Significantly higher TMB, TNB, ITH, and wCIN-score (P<0.001) were discovered in patients with HLA-LOH than without (*Figure 2G*). Moreover, the mutation frequencies of *TP53* (36.3% *vs.* 29.6%, P<0.01) (*Figure 2H*), *TTN* (45.4% *vs.* 20.3%, P<0.05) (*Figure 2I*), and *CSMD1* (36.3% *vs.* 5.5%, P<0.01) (*Figure 2J*) were significantly higher in HLA-LOH positive than the negative group.

A higher frequency of wCIN was observed in stage II and III patients with relapse than without (*Figure 2K*). No significant associations were found between TMB, TNB, ITH, or HLA-LOH and relapse status and disease stages. Higher TMB (log-rank test, P=0.02) (*Figure 2L*) and wCIN-score (log-rank test, P=0.03) (*Figure 2M*) predicted unfavorable DFS. Patients with low-TMB & high-ITH have significantly better prognoses than those with high-TMB & low-ITH (log-rank test, P=0.01) (*Figure 2N*). Multivariate Cox regression analysis adjusting for age, sex, and cTNM stages indicated that ITH was an independent prognostic factor (HR 0.196, 95% CI: 0.043–0.900, P=0.03), possibly because most included patients being early-stage (*Figure 2O*).

EGFR mutation status-related analyses

Recurrence probability was significantly higher in stage I patients with *EGFR* mutation than without (P<0.05) (*Figure 2P*). A trend of unfavorable prognosis of patients with *EGFR* mutation was observed, whereas without statistical significance (*Figure 2Q*). In descending order, the DFS days concerning *EGFR* mutation status were wild-type, L858R, other mutation types, and 19Del (*Figure 2R*). Moreover, patients with *EGFR* mutation and median-to-high-TMB correlated with significantly shorter DFS than those with low-TMB and without EGFR mutation (log-rank test, P<0.001) (*Figure 2S*). Higher TMB, TNB, and ITH were found in wild-type *EGFR* versus mutant *EGFR* individuals (*Figure 2T*). Additionally, the mutation frequencies of *PEG3* (*Figure 2U*) and *STK11* (*Figure 2V*) were significantly higher in wild-type than in mutant EGFR patients.

Transcriptional landscape of early-stage Ns-NSCLC

Significantly higher expression levels of *KDM5D*, *NLGN4Y*, and *PRAME* were found in ever-smokers than never-smokers (*Figure 3A*), which have been reported to correlate with tobacco use (42-44). Enhanced DNA repair, replication and methylation pathway activities and attenuated cell adhesion and epithelium development pathway activities were further identified in ever-smokers (*Figure 3B*), indicative of the carcinogenic effects of tobacco (45). Altogether, one hundred and forty-three DEGs were identified in patients with recurrence than without (*Figure 3C*), which were associated with upregulated mitotic pathway activity and downregulated immune-related pathways activity (*Figure 3D*).

A total of 140 up-regulated genes and 251 down-

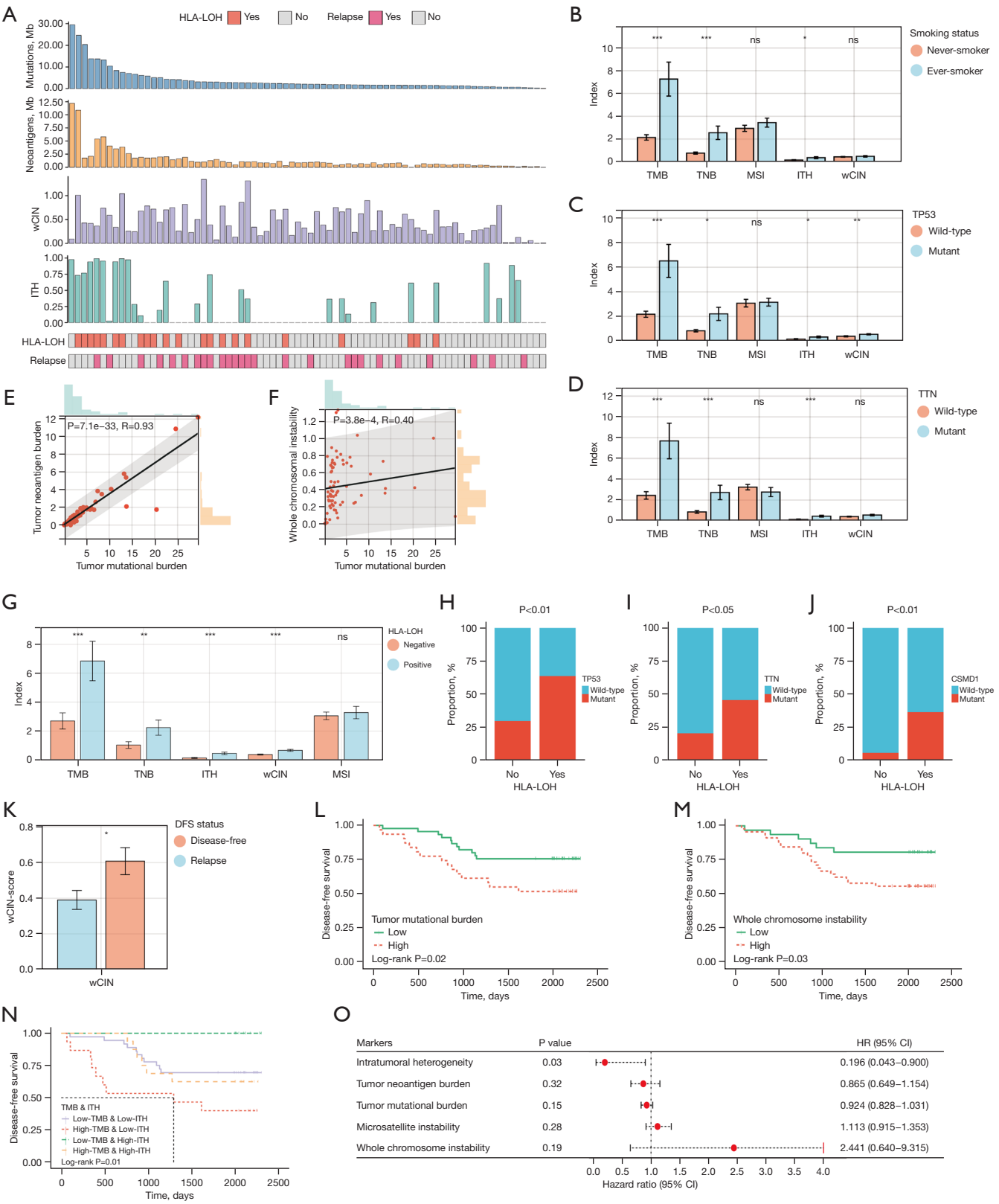

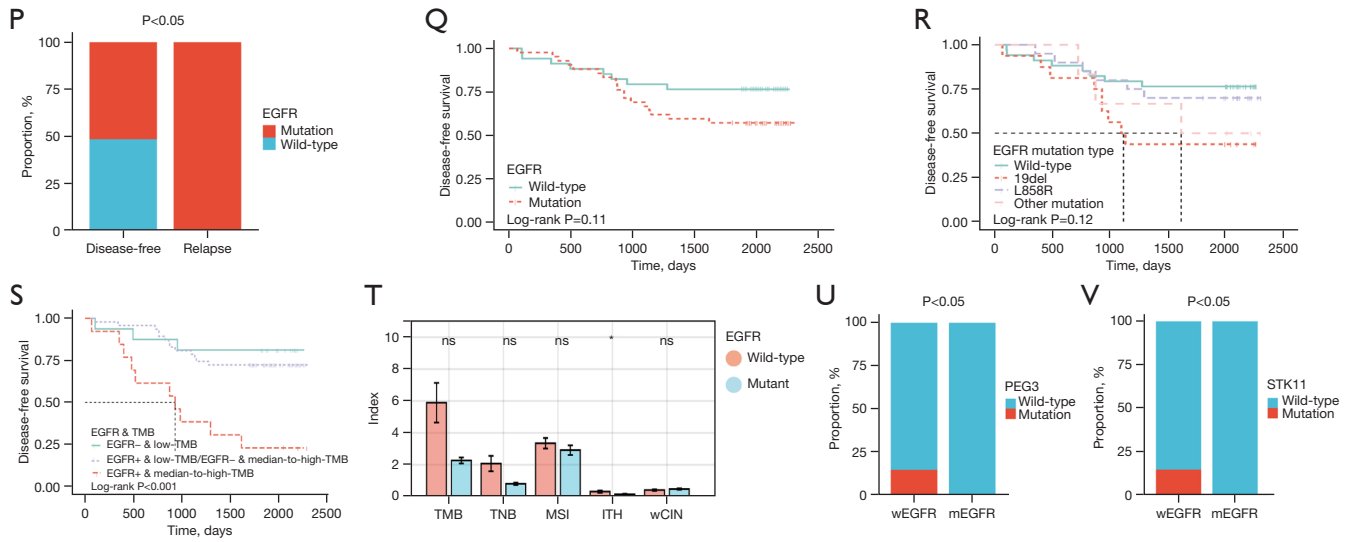

Figure 2 Genomic biomarker spectrums of Chinese early-stage non-squamous NSCLC. Genomic biomarker landscapes, including TMB, TNB, wCIN, ITH, and HLA-LOH of each patient, with relapse status as an annotation (A). Genomic biomarker spectrum differences concerning smoking status (B), driver gene mutations (C,D,T), and HLA-LOH status (G). Genomic biomarkers of TMB-TNB (E) and TMB-wCIN (F) demonstrated strong correlations. Higher mutation frequencies of *TP53* (H), *TTN* (I), and *CSMD1* (J) were observed in patients with HLA-LOH. A higher wCIN-score was discovered in patients with relapse than without (K). Prognostic significance of TMB (L), wCIN (M), and TMB & ITH combination (N) as evaluated by log-rank test. Prognostic effects of genomic biomarkers as evaluated by multivariate Cox regression analysis (O). Mutation frequency of *EGFR* between stage I patients with or without relapse (P). Disease-free survival differences concerning *EGFR* mutation status (Q) and mutation subtypes (R). Prognostic effects of *EGFR* and TMB combination category (S). Co-concurrent variants of *PEG3* (U) and *STK11* (V) in patients with or without *EGFR* mutation. The horizontal bar inside the boxes represents the median, and the lower and upper ends of the boxes are the first and third quartiles. Comparison of continuous data by Kruskal-Wallis test, *, P<0.05; **, P<0.01; ***, P<0.001; ns, non-significant. HLA-LOH, human leukocyte antigen loss of heterozygosity; wCIN, whole chromosomal instability; ITH, intratumoral heterogeneity; TMB, tumor mutational burden; TNB, tumor neoantigen burden; MSI, microsatellite instability; DFS, disease-free survival; HR, hazard ratio; CI, confidence interval; wEGFR, wild-type *EGFR*; mEGFR, mutated *EGFR*; NSCLC, non-small cell lung cancer.

regulated genes were discovered in stage II–III compared with stage I samples (*Figure 3E*). The DEGs were enriched into up-regulation of cell growth processes like cell cycle and DNA replication pathways, whereas downregulated cell adhesion and differentiation pathways were observed (*Figure 3F*), indicating the augmented invasive capacity of tumor cells (46). A total of 106 DEGs were found in *EGFR* mutation than wild-type patients (*Figure 3G*), which were also correlated with augmented mitotic cell cycle pathway activity and muted cell adhesion activity (*Figure 3H*), suggesting higher invasion and metastasis capacity.

We subsequently sought to evaluate the prognostic effects of these genes. Firstly, 2,483 immune-related genes were extracted referring to the ImmPort database (47), among which 1,443 genes were differentially expressed between tumor nest (TN) and paratumor tissue in our cohort (Table S4). Univariate Cox regression analysis further identified 65 genes with prognostic effects, which were used as candidate genes (Table S5). Subsequently, the least absolute shrinkage and selection operator (LASSO) Cox regression model was employed to select the robust prognosticators among the candidate factors (*Figure 3I,3J*). Eventually, a total of 14 genes, including *KLRD1*, *NCR1*, *ICAM2*, *TRIM22*, *PI3*, *INHBB*, *IGHG3*, *SPP1*, *CRABP2*, *PLAUR*, *ULBP2*, *IL31RA*, *GDF5*, and *IL1A* were screened out (*Figure 3K*). Up-regulation of *KLRD1*, *NCR1*, *ICAM2*, *TRIM22*, *PI3*, *INHBB*, and *IGHG3* was associated with better DFS, whereas up-regulation of *SPP1*, *CRABP2*, *PLAUR*, *ULBP2*, *IL31RA*, *GDF5*, and *IL1A* predicted the unfavorable DFS. Up-regulation of *CRABP2* (HR 1.163, 95% CI: 1.010–1.339, P=0.03), *ULBP2* (HR 1.552, 95% CI: 1.049–2.296, P=0.02), *IL31RA* (HR 1.809, 95% CI:

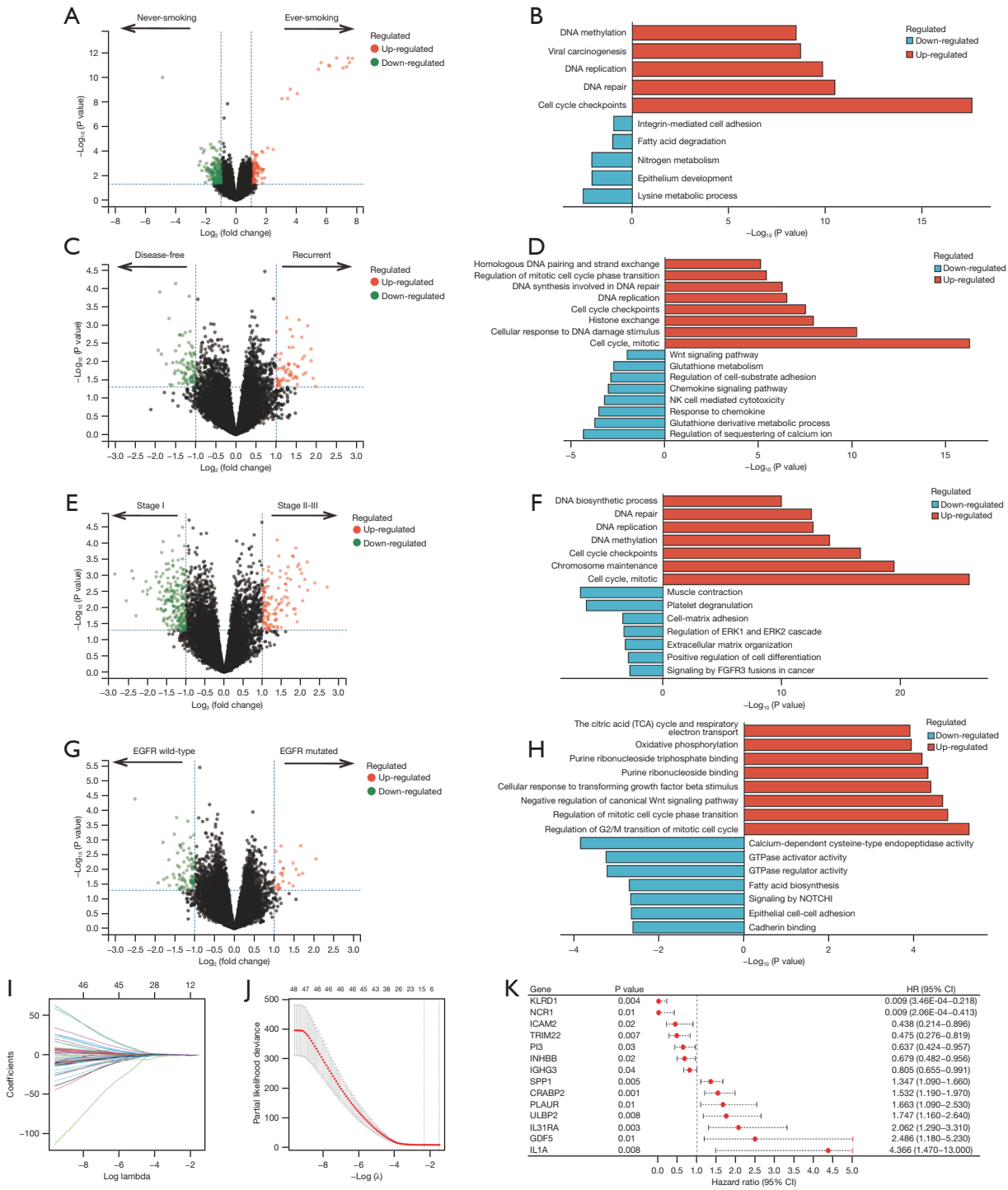

Figure 3 Transcriptomic spectrums of early-stage non-squamous non-small cell lung cancer. Differentially expressed genes and corresponding enriched pathways of ever-smokers *vs.* never-smokers (A,B), recurrent *vs.* disease-free (C,D), stage II–III *vs.* stage I (E,F), EGFR-mutated *vs.* wild-type (G,H). The LASSO Cox regression model screened out robust prognosticators among immune-related genes (I,J), and their prognostic effects were evaluated by the univariate Cox regression analysis (K). Red and green dots refer to significantly up-regulated and down-regulated genes, respectively. Black dots represent genes with insignificant changes in expression levels. NK, natural killer; HR, hazard ratio; CI, confidence interval; LASSO, least absolute shrinkage and selection operator.

1.096–2.985, P=0.02), and *IL1A* (HR 5.438, 95% CI: 1.626–18.184, P=0.006) also independently correlated with dismal DFS in the multivariate Cox setting.

Immune infiltration landscape of early-stage Ns-NSCLC

In the tumor tissues, the CIBERSORT approach showed that infiltration of activated memory CD4$^+$ T cells increased with TMB (*Figure 4A*) while infiltrating naïve B cells increased with TNB (*Figure 4B*). Lower memory B cell, neutrophil and higher plasma cell infiltrates were found in patients with HLA-LOH than without (*Figure 4C*). Infiltration of CD8$^+$ T cells, activated memory CD4$^+$ T cells, and naïve B cells was significantly lower in patients with EGFR mutation than without (*Figure 4D*), indicating impaired antitumor immunity. Lower infiltrating levels of CD8$^+$ T cell and higher Treg infiltrates were observed in patients with relapse than without (*Figure 4E*). Enriched plasma cells, CD8$^+$ T cells, and resting mast cells in TN were observed in patients without relapse. Compared with stage II–III, TME in stage I was featured by higher infiltrating immune effector cells like plasma cells, CD8$^+$ T cells, resting CD4$^+$ memory T cells, and lower infiltrating Tregs (*Figure 4F*), indicative of the "immune-hot" TME. Similar findings were validated by the MCP-counter approach (Figure S3A-S3F).

In the paratumor tissues, significantly lower CD8$^+$ T cell and activated NK cell infiltrates were found in patients with relapse than without. Moreover, *EGFR* mutation correlated with higher Tregs and lower CD8$^+$ T cells infiltration, indicating underactive TME. Interestingly, the infiltrating levels of M0 macrophages and resting DC increased with TMB and TNB levels, suggesting higher immunogenicity (Figure S3G-S3L).

The immune infiltration landscapes in the tumor and paratumor tissues were subsequently compared. Higher plasma cell, Treg, and M2 macrophage infiltrates were discovered in the tumor tissue. In contrast, higher infiltrating levels of CD8$^+$ T cells, activated NK cells, and activated CD4$^+$ memory T cells were found in the paratumor tissue (Figure S3M). Overall, immune-enriched TME was presented in early-stage Ns-NSCLC, and paratumor tissue seemed to hold higher immunoactivity than in tumor tissue.

Eventually, an unsupervised K-means clustering method via the Canberra metric was utilized to characterize the immune landscape of early-stage Ns-NSCLC (38). The TME could be generally classified into two major groups: tumor-inflamed and stroma-inflamed (*Figure 4G*). The stroma-inflamed group was characterized by high infiltrates of immune effector cells in paratumor tissue, including activated NK cells, activated CD4$^+$ memory T cells, and CD8$^+$ T cells, indicative of active immune response. Inversely, the tumor-inflamed group contained enriched M2 macrophages, Tregs and follicular helper T cells in tumor tissue, suggesting an immunosuppressive milieu.

TCR repertoire diversity spectrum

The mean values of observedDiversity, chaoE, d50Index, and normalizedShannonWienerIndex were utilized to compare the TCR repertoire diversity. The TCR repertoire was highest in PBMC, followed by tumor and paratumor tumor tissues (*Figure 5A,5B*). As for the TCR repertoire of PBMCs, decreased d50Index was observed in stage II–III compared with stage I samples (*Figure 5C*). Mutation in *TP53* indicated higher normalizedShannonWienerIndex, suggesting enhanced TCR diversity (*Figure 5D*). Inversely, mutations in *EGFR* and *ALK* correlated with muted TCR diversity (*Figure 5E,5F*). Insignificant differences in TCR diversity were found between different mutation types of *EGFR*.

As for the TCR repertoire of tumor tissue, augmented TCR diversity was demonstrated in ever-smokers than non-smokers (*Figure 5G*). Concerning the TCR repertoire of paratumor tissue, higher d50Index predicted significantly longer DFS (log-rank test, P=0.005) (*Figure 5H*), whereas higher normalizedShannonWienerIndex correlated with unfavorable prognosis (log-rank test, P=0.004) (*Figure 5I*). Higher inverseSimpsonIndex predicted significantly longer DFS (log-rank test, P=0.03) than lower ones (*Figure 5J*). Nevertheless, none of the above metrics used to estimate TCR repertoire diversity significantly correlated with DFS in the multivariate Cox analysis.

Prognostic effects of the individual omics/biomarker

The cTNM stage (AUC 0.727, 95% CI: 0.606–0.847) independently showed predictive capacity of DFS (*Figure 6A*). Among the genomic features, wCIN (AUC 0.630, 95% CI: 0.499–0.762) showed the highest predictive AUC, followed by TMB (AUC 0.588, 95% CI: 0.456–0.719) and microsatellite instability (MSI) (AUC 0.558, 95% CI: 0.420–0.695) (*Figure 6B-6H*). Among the transcriptomic characteristics, *KLRD1* (AUC 0.730, 95% CI: 0.616–0.844) showed the highest effectiveness, followed by *NCR1* (AUC 0.701, 95% CI: 0.573–0.830) and *PI3* (AUC 0.701, 95% CI: 0.577–0.824). None of the AUC values of TCR repertoire

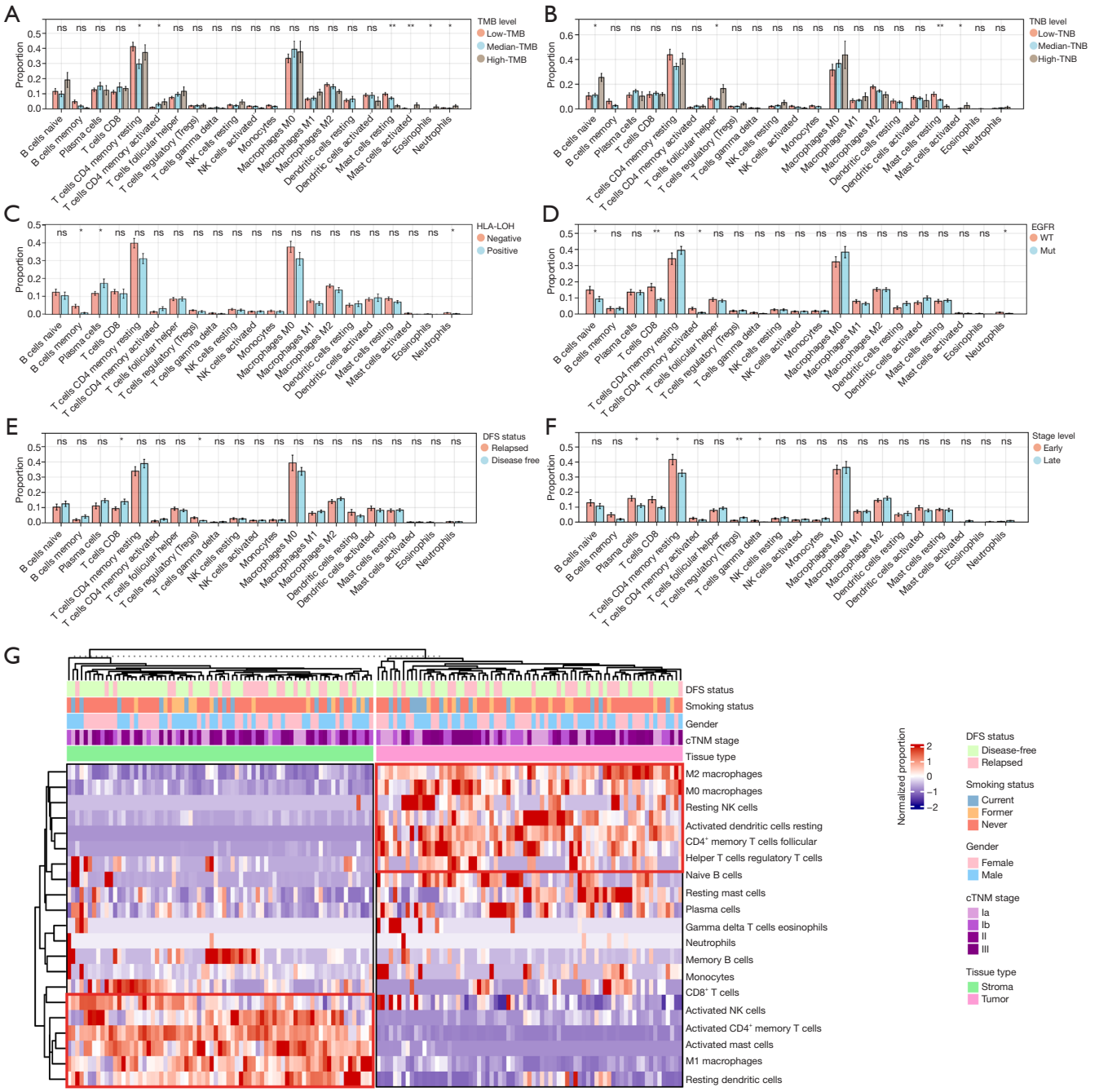

Figure 4 Immune infiltration landscapes in the tumor nest of early-stage Ns-NSCLC. Immune infiltration differences between different tumor mutational burden levels (A), tumor neoantigen burden levels (B), human leukocyte antigen loss of heterozygosity status (C), EGFR mutation status (D), disease-free survival status (E), and cTNM stage level (F), as evaluated by the CIBERSORT algorithm. The K-means clustering method identified two major immune subtypes of early-stage Ns-NSCLC (G). Comparison of continuous data by Kruskal-Wallis test. *, P<0.05; **, P<0.01; ns, non-significant. NK, natural killer; TMB, tumor mutational burden; TNB, tumor neoantigen burden; HLA-LOH, human leukocyte antigen loss of heterozygosity; Ns-NSCLC, non-squamous non-small cell lung cancer; WT, wild-type; Mut, mutant; DFS, disease-free survival; cTNM, clinical tumor staging.

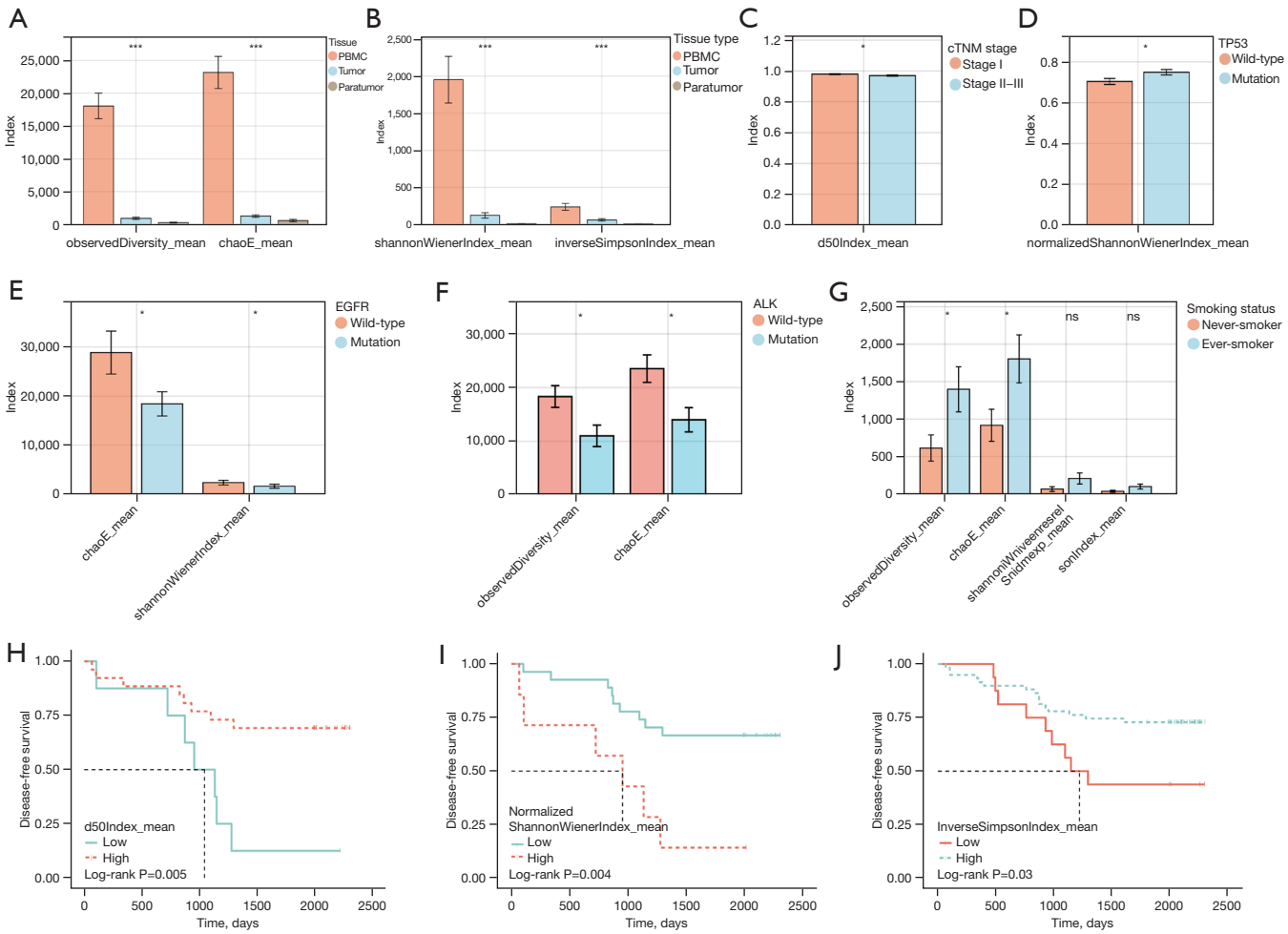

Figure 5 TCR repertoire spectrums of early-stage Ns-NSCLC. TCR repertoire diversity differences among peripheral blood, tumor, and paratumor samples (A,B). TCR repertoire diversity differences concerning cTNM stage (C), *TP53* (D), *EGFR* (E), and *ALK* (F) mutation status and smoking status (G). The prognostic effects of TCR repertoire diversity, including d50Index (H), normalizedShannonWienerIndex (I), and inverseSimpsonIndex (J). Comparison of continuous data by Kruskal-Wallis test, *, P<0.05; ***, P<0.001; ns, non-significant. PBMC, peripheral blood mononuclear cells; cTNM, clinical tumor staging; TCR, T-cell receptor; Ns-NSCLC, non-squamous non-small cell lung cancer.

biomarkers exceeded 0.6, with the highest of d50Index (AUC 0.590, 95% CI: 0.446–0.733). Consequently, individual omics/biomarker held limited performance to distinguish patients more prone to relapse (Figure S4).

Development of the multi-omics prognostic signature

Due to the unsatisfied performance of the individual omics/biomarker, we further developed the multi-omics prognostic signature (*Figure 6I*). We discovered that the integration of genomic, transcriptomic, clinical, and TCR repertoire features achieved stable and accurate efficacy across the seven methods in the training group (AUC =0.973, 1.000, 0.986, 0.904, 0.869, 1.000, and 0.735 of DTC, ETC, GBC, GPC, KNN, RF, and SVM, respectively) (*Figure 6J*). Feature importance analyses further demonstrated that GDF5 expression, cTNM stage, *PLAUR* expression, *IL31RA* expression, and normalizedShannonWienerIndex were the dominant features (*Figure 6K*), and RNA features held the largest contribution generally in the RF model. Given the generalization of NGS in clinical practice, we further interrogated whether Clinical + RNA or Clinical + DNA characteristics could reach comparable performance. Surprisingly, both combinations showed precise and stable

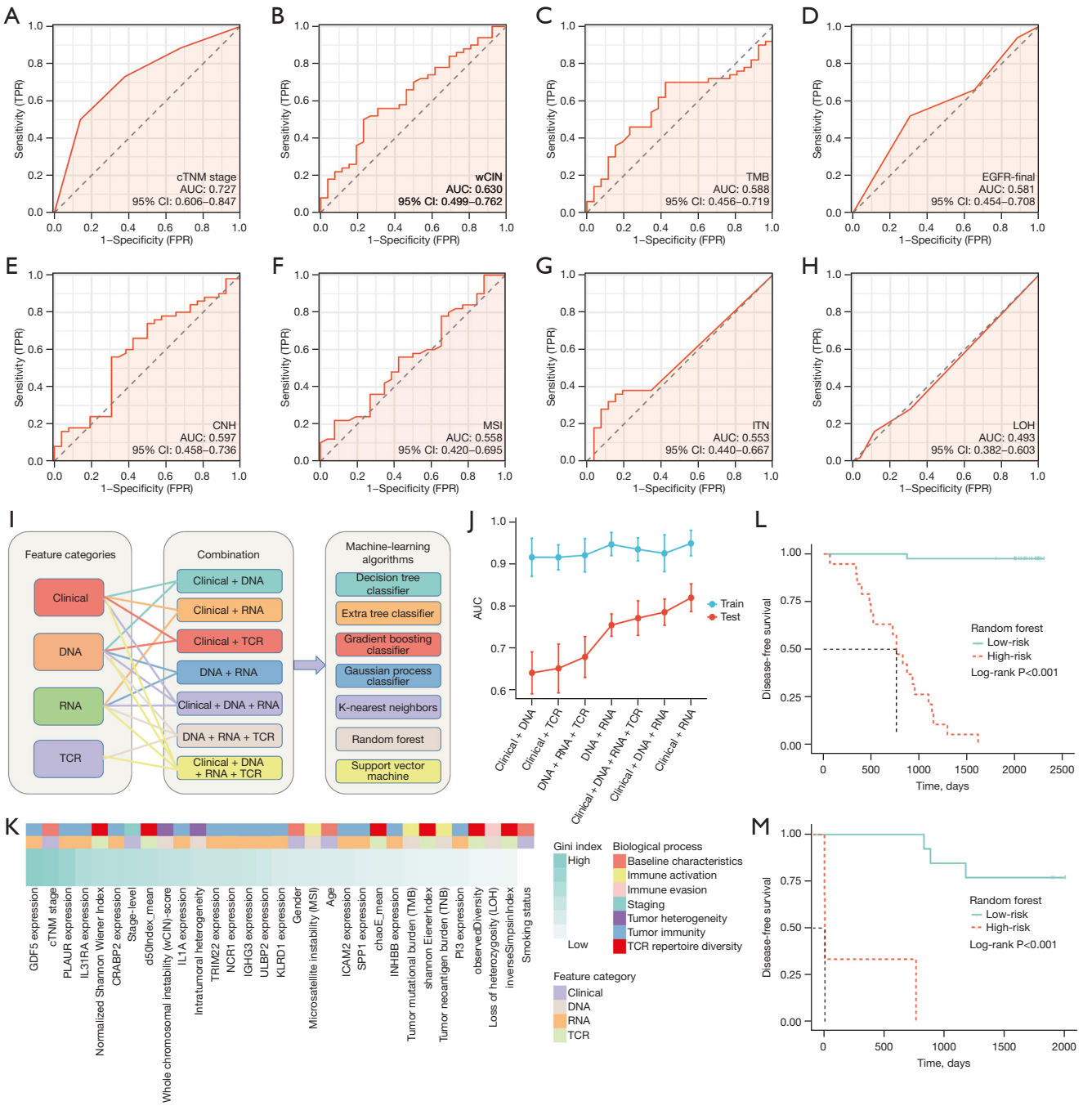

Figure 6 Construction and validation of multi-omics prognostic model based on clinicopathological, genomic, transcriptomic, and T-cell receptors repertoire sequencing data. The predictive accuracy of individual omics/biomarker, including clinicopathological characteristics (A) and genomic biomarkers (B-H). Flowchart demonstrating the process of establishing a multi-omics prognostic model via machine-learning approaches (I). Predictive accuracy of multi-omics prognostic model based on different combination categories in the training and testing cohort (J). Feature importance analyses as evaluated by the Gini index of the RF model combining four omics categories (K). DFS differences predicted by the RF algorithm in the training (L) and testing (M) cohorts. TPR, true positive rate; FPR, false positive rate; cTNM, clinical tumor staging; wCIN, whole chromosomal instability; TMB, tumor mutational burden; CNH, copy number high; MSI, microsatellite instability; ITH, intratumoral heterogeneity; LOH, loss of heterozygosity; AUC, area under the curve; CI, confidence interval; TCR, T-cell receptor; RF, random forest; DFS, disease-free survival.

predictive performance (Clinical + RNA: AUC =0.978, 1.000, 0.998, 0.999, 0.815, 0.975, and 0.818 of DTC, ETC, GBC, GPC, KNN, RF, and SVM, respectively; Clinical + DNA: AUC =0.999, 0.988, 1.000, 0.997, 0.803, 0.936, and 0.829 of DTC, ETC, GBC, GPC, KNN, RF, and SVM, respectively).

We then validated these algorithms in the internal testing cohort, showing that the Clinical + RNA features combination reached the most stable and accurate performance generally (AUC =0.692, 0.933, 0.800, 0.733, 0.867, 0.833, and 0.900 of DTC, ETC, GBC, GPC, KNN, RF, and SVM, respectively). The ACC, precision, recall, F1-score, and AUC of the seven combination categories across the seven ML algorithms in the training and testing cohort are listed in Tables S6,S7.

Given that the Clinical + RNA features combination of the RF algorithm exhibited stabler and more accurate performance than other ML methods (AUC 0.975, 95% CI: 0.926–1.000 in the training cohort; AUC 0.833, 95% CI: 0.627–1.000 in the testing cohort), it was chosen to be the ultimate predictor. The RF algorithm showed better AUC than the cTNM stage across the seven combination categories (Clinical features + DNA: P=0.14; Clinical features + RNA: P<0.001; Clinical features + TCR: P=0.26; Clinical features + DNA + RNA: P=0.05; Clinical features + DNA + RNA + TCR: P<0.001; DNA + RNA: P<0.001; DNA + RNA + TCR: P<0.001). The predicted high-risk early-stage Ns-NSCLC population held significantly shorter DFS in training (*Figure 6L*) and testing (*Figure 6M*) cohort (P<0.001).

Discussion

Our study pinpointed the unique molecular and immune alterations in the Chinese early-stage Ns-NSCLC cohort, which may affect prognosis and influence the crosstalk between tumor and the immune system, unveiling novel cancer biological meanings.

Our WES analysis identified consistent findings which were previously reported on the East-Asian Ns-NSCLC population. For instance, *EGFR* was the most frequently mutated gene and C > A base substitution was more frequently detected in ever-smokers (48). Frequently mutated smoking-related SBS4 signature was also detected, which has been reported to be the major feature of smoker LCs. Besides, different driver genes mutations may predict inverse somatic mutational burden (43).

Besides corroborating previous findings, several novel genomic alterations in recurrent early-stage Ns-NSCLC were discovered. For instance, a higher mutation rate of FGD5 was found in recurrent patients, which has been postulated to maintain breast cancer stem cell characteristics and facilitate tumor development (49), whereas no relevant findings on Ns-NSCLC were found. A higher mutation frequency of *FLT4* was also discovered, which may activate the PI3K-AKT pathway to promote the angiogenesis of LUAD (50). Besides, a higher mutation frequency of *MYO18B*, a tumor suppressor gene (51), was identified in recurrent samples, and it was also a negative predictor of DFS. Mutations in *MUC17*, *ABCA2*, and *PDE4DIP* were also accentuated to play an important role in prognosis. Functional analyses further suggested that the mutation of these genes correlated with augmented malignant transformation of cells, warranting future experimental studies to examine the underlying biological implications.

As for the sCNA spectrum, alterations in cytobands of chr4p, chr8q, chr14q, etc., demonstrated significant variation of Del or Amp. Significant Amps in 8q24.3, 14q13.1, 14q11.2, and Del in 3p21.1 were highlighted in early-stage recurrent Ns-NSCLC. Amp in 14q13.1 has been postulated to be the oncogenic alteration of pulmonary lymphoepithelioma-like carcinoma, a rare subtype of NSCLC (52). Besides, *PSCA* at 8q24.3 is among the most frequently detected gastric cancer-susceptibility genes (53). Del in 3p21.1 has been reported to correlate with metastasis of renal and pancreatic cancer (54) while it was first described in Ns-NSCLC. Concerning disease-free samples, cytoband Amp in the chr7q22.1 region was found, which included the *COL1A2* gene, and it has been postulated to correlate with extracellular matrix-receptor interaction in esophageal cancer (55). Amp in the chr8q24.21 that included the *MYC* gene was also found. And MYC is a classical oncogene crucial for tumor evolution and immune evasion in TME, mainly relating to Wnt/β-catenin signal pathways (56). Overall, our findings supplemented the repertoire of candidate genomic alterations contained in Ns-NSCLC pathogenesis.

We comprehensively depicted the spectrum of genomic biomarkers of early-stage Ns-NSCLC, including TMB, TNB, ITH, HLA-LOH, and wCIN. The occurrence of HLA-LOH was 28.9%, similar to a recent report of the Chinese NSCLC cohort (23.8%) (38). HLA-LOH was associated with higher mutation frequencies of classical oncogene *TP53* and immune-related genes like *TTN* and *CSMD1*. In the context of inconsistent findings concerning the role of HLA-LOH in predicting ICI response (57), combining HLA-LOH status with concurrent mutated

gene signatures, especially immune-related ones, may reach better performance. Moreover, HLA-LOH predicted higher TMB, TNB, ITH, and wCIN-score, suggesting higher mutational burden and a greater probability of tumor immune escape. Mutations in *TP53* and *TTN* correlated with higher TMB and TNB, representing higher immunogenicity. Higher incidences of HLA-LOH, higher TMB and TNB were identified in ever-smokers than never-smokers, recapitulating previous findings.

We subsequently investigated the associations between various biomarkers, either alone or in combination, with prognosis. We found that higher TMB and wCIN-score predicted unfavorable DFS. On the contrary, higher ITH was an independent predictor of better DFS in early-stage Ns-NSCLC, showing the opposite effect from a previous study that focused on advanced NSCLC (22). Interestingly, low-TMB & high-ITH correlated with significantly longer DFS than those with high-TMB & low-ITH, implying combining the characteristics of subclonal mutations and immunogenic neoantigens may better achieve risk stratification. Besides, patients who harbored EGFR mutation and median-to-high TMB held worse DFS than those with low TMB and without EGFR mutation, corroborating previous reports (58).

Transcriptomic analysis underscored higher cell cycle pathway activity and lower cell differentiation and adhesion activity in recurrent, relatively advanced-stage, smokers, and *EGFR*-mutated Ns-NSCLC, mirroring the accumulation of cancer cell invasion and metastasis capacity that empowered the immune escape. The expression patterns of immune-related genes were fully assessed, pinpointing several essential prognosticators of early-stage Ns-NSCLC. *CRABP2*, i.e., cellular retinoic acid-binding protein, has been reported to facilitate LC metastasis by integrin β1/FAK/ERK pathway of *in vitro* model (59). Likewise, up-regulation of *CRABP2* was discovered in TN than paratumor tissue, and it was an independent prognosticator of unfavorable DFS, suggesting a potential target to improve prognosis. *ULBP2*, a ligand of *NKG2D* that usually expresses under tissue stress or injury, is an important target of immune surveillance and a trigger of antitumor immunity. We found that the expression level of *ULBP2* was significantly higher in TN than in paratumor tissue, and it correlated with dismal DFS, consistent with a previous study by Yamaguchi and colleagues (60). Additionally, up-regulated *IL1A*, a cytokine with pleiotropic functions in tumor evolution, portended a significantly worse prognosis. However, we could not further determine the cellular sources of expression of these genes and their correlations with other known druggable targets like by single-cell RNA sequencing (61) and multiplex immunofluorescence (62).

Via the deconvolution algorithm, phenotypic heterogeneity in TME was observed, and two major subtypes, including the tumor-inflamed and stroma-inflamed groups, were generated. The stroma-inflamed group featured by high activated NK cell, $CD4^+$ T cell, and $CD8^+$ T cell infiltrates indicated the benefit of ICI treatment (63). On the contrary, the tumor-inflamed group exhibited enriched M2 macrophages and Tregs, indicating ICI plus therapy targeting specific cell lineage like macrophages may better work (64,65). Additionally, we also parsed the different TME landscapes concerning different genomic alteration patterns, benefiting from a multi-omics setting.

Through parsing the TCR repertoire spectrum, we found that driver gene mutations like *EGFR* and *ALK* predicted muted TCR diversity while mutation in tumor suppressor genes like *TP53* correlated with augmented TCR diversity inversely. Prognostic effects of TCR diversity of PBMCs were noted, demonstrating a noninvasive method for relapse surveillance.

Studies using other different omics also succeeded in predicting the prognosis and immunotherapy response of cancers. For instance, Triozzi and colleagues developed a metabolomic signature that correlated with glycolysis to characterize the ICI responders of melanoma (66). Moreover, they also found that higher extracellular acidification rate and lactate-to-pyruvate ratio were prognostic of superior outcomes. Proteomics narrows the gap between cancer genotypes and phenotypes and has paved the way for precision oncology in recent years. Recently, Harel *et al.* proposed a predictive signature of ICI response of NSCLC based on plasma proteomic profiling, including *CXCL8* and *CXCL10* proteins (67).

Eventually, seven ML algorithms were employed to estimate the predictive accuracy of seven combination categories based on clinical, genomic, transcriptomic, and TCR repertoire data. Clinical and RNA features combination in the RF algorithm, with AUC of 97.5% and 83.3% in the training and testing cohort, respectively, significantly outperformed other methods. Consequently, the model was robust and had the potential to optimize risk stratification of early-stage Ns-NSCLC along with the increased clinical utility of target panel sequencing. More importantly, such a framework underscored the significance of data integration via ML approaches for predicting relapse and may be feasible for other cancer types.

Several limitations should be noted. First, our study is restricted by the sample size and the number of individuals with specific mutant genes. In this sense, the generated hypotheses on the effects of molecular alterations on prognosis need to be examined in other populations or cohorts. Second, the immune subtypes of early-stage Ns-NSCLC were inferred from the deconvolution algorithm of RNA-seq data and lacked validation at the protein level, like by multiplex immunofluorescence (62). Third, while diversity, clonality, and similarity are the essential features of TCR repertoire, only diversity was probed. Moreover, the proposed multi-omics prognosticator held the risk of over-fitting due to limited cohort size and a lack of validation in the external cohort.

In recent years, numerous novel omics techniques have empowered researchers to dissect the pathogenesis of cancers at unprecedented resolution and scale, demonstrating a holistic view of cancer biology. Multi-omics analyses also pose the potential to identify innovative druggable targets and biomarkers for optimizing treatment benefits. The advent of multi-layer and broader data also raises the challenges of better synthesizing them and generalizing the findings into clinical utility. In our view, first, the employment of ML/deep learning algorithms, which could capture complex high-dimensional associations of multimodality data, is imperative. Second, technical specification and standardization across different labs to establish reproducible data are indispensable. Third, prospective and cross-cohort validation examining the associations or causalities between experimental findings and clinical outcomes are requisite. Overall, great efforts are underway to dissect the heterogeneity and plasticity of tumors, and we anticipate their integration into precision oncology.

Conclusions

In brief, this study comprehensively profiled the genomic, transcriptomic, and TCR repertoire spectrums of Chinese early-stage Ns-NSCLC, shedding light on biological underpinnings and candidate biomarkers for prognosis development.

Acknowledgments

Funding: This work was supported by National Natural Science Foundation of China (No. 81871893); Key Project of Guangzhou Scientific Research Project (No. 201804020030); Cultivation of Guangdong College Students' Scientific and Technological Innovation ("Climbing Program" Special Funds) (Nos. pdjh2020a0480, pdjh2021a0407).

Footnote

Reporting Checklist: The authors have completed the TRIPOD reporting checklist. Available at https://tlcr.amegroups.com/article/view/10.21037/tlcr-23-800/rc

Data Sharing Statement: Available at https://tlcr.amegroups.com/article/view/10.21037/tlcr-23-800/dss

Peer Review File: Available at https://tlcr.amegroups.com/article/view/10.21037/tlcr-23-800/prf

Conflicts of Interest: All authors have completed the ICMJE uniform disclosure form (available at https://tlcr.amegroups.com/article/view/10.21037/tlcr-23-800/coif). W.L. serves as an unpaid Associate Editor-in-Chief of *Translational Lung Cancer Research* from May 2023 to April 2024. Xiaoli Cui, D.W., Z.G., and H.L. are current employees of YuceBio Technology Co., Ltd. The other authors have no conflicts of interest to declare.

Ethical Statement: The authors are accountable for all aspects of the work in ensuring that questions related to the accuracy or integrity of any part of the work are appropriately investigated and resolved. Informed consent of included patients was obtained, and this research was approved by the First Affiliated Hospital of Guangzhou Medical University Ethics Committee (approval No. KLS-17-03). The study was conducted in accordance with the Declaration of Helsinki (as revised in 2013).

References

1. Sung H, Ferlay J, Siegel RL, et al. Global Cancer Statistics 2020: GLOBOCAN Estimates of Incidence and Mortality

Worldwide for 36 Cancers in 185 Countries. CA Cancer J Clin 2021;71:209-49.
2. Miller M, Hanna N. Advances in systemic therapy for non-small cell lung cancer. BMJ 2021;375:n2363.
3. Li C, Wang H, Jiang Y, et al. Advances in lung cancer screening and early detection. Cancer Biol Med 2022;19:591-608.
4. Jonas DE, Reuland DS, Reddy SM, et al. Screening for Lung Cancer With Low-Dose Computed Tomography: Updated Evidence Report and Systematic Review for the US Preventive Services Task Force. JAMA 2021;325:971-87.
5. Taylor MD, Nagji AS, Bhamidipati CM, et al. Tumor recurrence after complete resection for non-small cell lung cancer. Ann Thorac Surg 2012;93:1813-20; discussion 1820-1.
6. Devarakonda S, Morgensztern D, Govindan R. Genomic alterations in lung adenocarcinoma. Lancet Oncol 2015;16:e342-51.
7. Cancer Genome Atlas Research Network. Comprehensive genomic characterization of squamous cell lung cancers. Nature 2012;489:519-25.
8. Zhang T, Joubert P, Ansari-Pour N, et al. Genomic and evolutionary classification of lung cancer in never smokers. Nat Genet 2021;53:1348-59.
9. Rooney M, Devarakonda S, Govindan R. Genomics of squamous cell lung cancer. Oncologist 2013;18:707-16.
10. Kadara H, Choi M, Zhang J, et al. Whole-exome sequencing and immune profiling of early-stage lung adenocarcinoma with fully annotated clinical follow-up. Ann Oncol 2017;28:75-82.
11. Choi M, Kadara H, Zhang J, et al. Mutation profiles in early-stage lung squamous cell carcinoma with clinical follow-up and correlation with markers of immune function. Ann Oncol 2017;28:83-9.
12. Faruki H, Mayhew GM, Serody JS, et al. Lung Adenocarcinoma and Squamous Cell Carcinoma Gene Expression Subtypes Demonstrate Significant Differences in Tumor Immune Landscape. J Thorac Oncol 2017;12:943-53.
13. Li B, Cui Y, Diehn M, et al. Development and Validation of an Individualized Immune Prognostic Signature in Early-Stage Nonsquamous Non-Small Cell Lung Cancer. JAMA Oncol 2017;3:1529-37.
14. Kratz JR, He J, Van Den Eeden SK, et al. A practical molecular assay to predict survival in resected non-squamous, non-small-cell lung cancer: development and international validation studies. Lancet 2012;379:823-32.
15. Lahiri A, Maji A, Potdar PD, et al. Lung cancer immunotherapy: progress, pitfalls, and promises. Mol Cancer 2023;22:40.
16. Riaz N, Havel JJ, Makarov V, et al. Tumor and Microenvironment Evolution during Immunotherapy with Nivolumab. Cell 2017;171:934-949.e16.
17. Aran A, Garrigós L, Curigliano G, et al. Evaluation of the TCR Repertoire as a Predictive and Prognostic Biomarker in Cancer: Diversity or Clonality? Cancers (Basel) 2022;14:1771.
18. Han J, Duan J, Bai H, et al. TCR Repertoire Diversity of Peripheral PD-1(+)CD8(+) T Cells Predicts Clinical Outcomes after Immunotherapy in Patients with Non-Small Cell Lung Cancer. Cancer Immunol Res 2020;8:146-54.
19. Liu YY, Yang QF, Yang JS, et al. Characteristics and prognostic significance of profiling the peripheral blood T-cell receptor repertoire in patients with advanced lung cancer. Int J Cancer 2019;145:1423-31.
20. Ettinger DS, Wood DE, Aisner DL, et al. Non-Small Cell Lung Cancer, Version 3.2022, NCCN Clinical Practice Guidelines in Oncology. J Natl Compr Canc Netw 2022;20:497-530.
21. World Medical Association Declaration of Helsinki: ethical principles for medical research involving human subjects. JAMA 2013;310:2191-4.
22. Fang W, Jin H, Zhou H, et al. Intratumoral heterogeneity as a predictive biomarker in anti-PD-(L)1 therapies for non-small cell lung cancer. Mol Cancer 2021;20:37.
23. McGranahan N, Rosenthal R, Hiley CT, et al. Allele-Specific HLA Loss and Immune Escape in Lung Cancer Evolution. Cell 2017;171:1259-1271.e11.
24. Braun DA, Hou Y, Bakouny Z, et al. Interplay of somatic alterations and immune infiltration modulates response to PD-1 blockade in advanced clear cell renal cell carcinoma. Nat Med 2020;26:909-18.
25. Sanchez-Vega F, Mina M, Armenia J, et al. Oncogenic Signaling Pathways in The Cancer Genome Atlas. Cell 2018;173:321-337.e10.
26. Bray NL, Pimentel H, Melsted P, et al. Near-optimal probabilistic RNA-seq quantification. Nat Biotechnol 2016;34:525-7.
27. Subramanian A, Tamayo P, Mootha VK, et al. Gene set enrichment analysis: a knowledge-based approach for interpreting genome-wide expression profiles. Proc Natl Acad Sci U S A 2005;102:15545-50.
28. Laughney AM, Hu J, Campbell NR, et al. Regenerative lineages and immune-mediated pruning in lung cancer

metastasis. Nat Med 2020;26:259-69.
29. Barker DJ, Maccari G, Georgiou X, et al. The IPD-IMGT/HLA Database. Nucleic Acids Res 2023;51:D1053-60.
30. Bolotin DA, Poslavsky S, Mitrophanov I, et al. MiXCR: software for comprehensive adaptive immunity profiling. Nat Methods 2015;12:380-1.
31. Shugay M, Bagaev DV, Turchaninova MA, et al. VDJtools: Unifying Post-analysis of T Cell Receptor Repertoires. PLoS Comput Biol 2015;11:e1004503.
32. Newman AM, Liu CL, Green MR, et al. Robust enumeration of cell subsets from tissue expression profiles. Nat Methods 2015;12:453-7.
33. Becht E, Giraldo NA, Lacroix L, et al. Estimating the population abundance of tissue-infiltrating immune and stromal cell populations using gene expression. Genome Biol 2016;17:218.
34. Garfinkle R, Filion KB, Bhatnagar S, et al. Prediction model and web-based risk calculator for postoperative ileus after loop ileostomy closure. Br J Surg 2019;106:1676-84.
35. Riley RD, Ensor J, Snell KIE, et al. Calculating the sample size required for developing a clinical prediction model. BMJ 2020;368:m441.
36. Camp RL, Dolled-Filhart M, Rimm DL. X-tile: a new bio-informatics tool for biomarker assessment and outcome-based cut-point optimization. Clin Cancer Res 2004;10:7252-9.
37. Wang C, Yin R, Dai J, et al. Whole-genome sequencing reveals genomic signatures associated with the inflammatory microenvironments in Chinese NSCLC patients. Nat Commun 2018;9:2054.
38. Cancer Genome Atlas Research Network. Comprehensive molecular profiling of lung adenocarcinoma. Nature 2014;511:543-50.
39. Pfeifer GP. Environmental exposures and mutational patterns of cancer genomes. Genome Med 2010;2:54.
40. Liu Y, Gusev A, Heng YJ, et al. Somatic mutational profiles and germline polygenic risk scores in human cancer. Genome Med 2022;14:14.
41. Wang Z, Wang C, Lin S, et al. Effect of TTN Mutations on Immune Microenvironment and Efficacy of Immunotherapy in Lung Adenocarcinoma Patients. Front Oncol 2021;11:725292.
42. Saunders GRB, Wang X, Chen F, et al. Genetic diversity fuels gene discovery for tobacco and alcohol use. Nature 2022;612:720-4.
43. Huang Z, Sun S, Lee M, et al. Single-cell analysis of somatic mutations in human bronchial epithelial cells in relation to aging and smoking. Nat Genet 2022;54:492-8.
44. Duan Y, Du Y, Gu Z, et al. Expression, Prognostic Value, and Functional Mechanism of the KDM5 Family in Pancreatic Cancer. Front Cell Dev Biol 2022;10:887385.
45. Hecht SS. Cigarette smoking and lung cancer: chemical mechanisms and approaches to prevention. Lancet Oncol 2002;3:461-9.
46. Martínez-Ruiz C, Black JRM, Puttick C, et al. Genomic-transcriptomic evolution in lung cancer and metastasis. Nature 2023;616:543-52.
47. Shen S, Wang G, Zhang R, et al. Development and validation of an immune gene-set based Prognostic signature in ovarian cancer. EBioMedicine 2019;40:318-26.
48. Chen J, Yang H, Teo ASM, et al. Genomic landscape of lung adenocarcinoma in East Asians. Nat Genet 2020;52:177-86.
49. Li K, Zhang TT, Zhao CX, et al. Faciogenital Dysplasia 5 supports cancer stem cell traits in basal-like breast cancer by enhancing EGFR stability. Sci Transl Med 2021;13:eabb2914.
50. Fang H, Sun Q, Zhou J, et al. m(6)A methylation reader IGF2BP2 activates endothelial cells to promote angiogenesis and metastasis of lung adenocarcinoma. Mol Cancer 2023;22:99.
51. Nishioka M, Kohno T, Tani M, et al. MYO18B, a candidate tumor suppressor gene at chromosome 22q12.1, deleted, mutated, and methylated in human lung cancer. Proc Natl Acad Sci U S A 2002;99:12269-74.
52. Chen B, Zhang Y, Dai S, et al. Molecular characteristics of primary pulmonary lymphoepithelioma-like carcinoma based on integrated genomic analyses. Signal Transduct Target Ther 2021;6:6.
53. Study Group of Millennium Genome Project for Cancer, Sakamoto H, Yoshimura K, et al. Genetic variation in PSCA is associated with susceptibility to diffuse-type gastric cancer. Nat Genet 2008;40:730-40.
54. Yang J, Lin P, Yang M, et al. Integrated genomic and transcriptomic analysis reveals unique characteristics of hepatic metastases and pro-metastatic role of complement C1q in pancreatic ductal adenocarcinoma. Genome Biol 2021;22:4.
55. Li G, Jiang W, Kang Y, et al. High expression of collagen 1A2 promotes the proliferation and metastasis of esophageal cancer cells. Ann Transl Med 2020;8:1672.
56. Dhanasekaran R, Deutzmann A, Mahauad-Fernandez WD, et al. The MYC oncogene - the grand orchestrator of cancer growth and immune evasion. Nat Rev Clin Oncol 2022;19:23-36.

57. Chowell D, Morris LGT, Grigg CM, et al. Patient HLA class I genotype influences cancer response to checkpoint blockade immunotherapy. Science 2018;359:582-7.
58. Offin M, Rizvi H, Tenet M, et al. Tumor Mutation Burden and Efficacy of EGFR-Tyrosine Kinase Inhibitors in Patients with EGFR-Mutant Lung Cancers. Clin Cancer Res 2019;25:1063-9.
59. Wu JI, Lin YP, Tseng CW, et al. Crabp2 Promotes Metastasis of Lung Cancer Cells via HuR and Integrin β1/FAK/ERK Signaling. Sci Rep 2019;9:845.
60. Yamaguchi K, Chikumi H, Shimizu A, et al. Diagnostic and prognostic impact of serum-soluble UL16-binding protein 2 in lung cancer patients. Cancer Sci 2012;103:1405-13.
61. Pullikuth AK, Routh ED, Zimmerman KD, et al. Bulk and Single-Cell Profiling of Breast Tumors Identifies TREM-1 as a Dominant Immune Suppressive Marker Associated With Poor Outcomes. Front Oncol 2021;11:734959.
62. Peng H, Wu X, Liu S, et al. Multiplex immunofluorescence and single-cell transcriptomic profiling reveal the spatial cell interaction networks in the non-small cell lung cancer microenvironment. Clin Transl Med 2023;13:e1155.
63. Peng H, Wu X, Zhong R, et al. Profiling Tumor Immune Microenvironment of Non-Small Cell Lung Cancer Using Multiplex Immunofluorescence. Front Immunol 2021;12:750046.
64. Yang L, Zhang Y. Tumor-associated macrophages: from basic research to clinical application. J Hematol Oncol 2017;10:58.
65. Wu XR, Peng HX, He M, et al. Macrophages-based immune-related risk score model for relapse prediction in stage I-III non-small cell lung cancer assessed by multiplex immunofluorescence. Transl Lung Cancer Res 2022;11:523-42.
66. Triozzi PL, Stirling ER, Song Q, et al. Circulating Immune Bioenergetic, Metabolic, and Genetic Signatures Predict Melanoma Patients' Response to Anti-PD-1 Immune Checkpoint Blockade. Clin Cancer Res 2022;28:1192-202.
67. Harel M, Lahav C, Jacob E, et al. Longitudinal plasma proteomic profiling of patients with non-small cell lung cancer undergoing immune checkpoint blockade. J Immunother Cancer 2022;10:e004582.

Cite this article as: Peng H, Wu X, Cui X, Liu S, Liang Y, Cai X, Shi M, Zhong R, Li C, Liu J, Wu D, Gao Z, Lu X, Luo H, He J, Liang W. Molecular and immune characterization of Chinese early-stage non-squamous non-small cell lung cancer: a multi-omics cohort study. Transl Lung Cancer Res 2024;13(4):763-784. doi: 10.21037/tlcr-23-800

Supplementary

Table S1 Details of kits used in the present study

Name	Company	Country
QIAamp DNA FFPE Tissue Kit	Qiagen	USA
DNeasy Blood and tissue Kit	Qiagen	USA
dsDNA HS Assay Kit	ThermoFisher Scientific	USA
KAPA Hyper Prep Kit	KAPA Biosystems	USA
xGen Exome Research Panel and Hybridization and Wash Reagents Kit	Integrated DNA Technology	USA
RNeasy Plus Universal Kit	Qiagen	USA
Qubit™ RNA HS Assay Kit	ThermoFisher Scientific	USA
Take 3	BioTek	USA
RNA Cartridge kit of the Qseq100 Bio-Fragment Analyzer	Bioptic	China
VAHTS mRNA-seq V3 Library Prep Kit	Vazyme	China

Table S2 Details of software used in the present study

Name	Version
SOAPnuke	1.5.6
Burrows-Wheeler Alignment tool	0.7.12
SAMtools	1.3
SAMBLASTER	0.1.22
VarScan	2.4.1
SnpEff	4.3
CNVkit	0.8.1
ascatNgs	3.1.0
POLYSOLVER	1.0
Bwakit	0.7.11
trim galore	0.6.7
Kallisto	0.46.2
Gencode	38.0
MiXCR	2.1.10
VDJtools	1.2.1
PyClone	0.13.0

https://dx.doi.org/10.21037/tlcr-23-800

Table S3 Detailed information on hyperparameter combinations per model

Model	Hyperparameter combinations
Support vector machine	kernel: ['linear'], C: [0.1, 1, 10]
Random forest	n_estimators: randint(100, 1000), max_depth: randint(5, 20), min_samples_split: randint(2, 10), min_samples_leaf: randint(1, 10), max_features: ['auto', 'sqrt'], bootstrap: [True, False]
Gradient boosting classifier	n_estimators: [50, 100, 200], learning_rate: [0.1, 0.01, 0.001], max_depth: [4]
Decision tree classifier	max_depth: [None, 5, 10, 15], min_samples_split: [2, 5, 10], min_samples_leaf: [1, 2, 3]
Extra tree classifier	n_estimators: [100, 200, 300], max_depth: [None, 5, 10], min_samples_split: [2, 5, 10]
Gaussian process classifier	kernel = 1.0 *RBF(1.0, length_scale_bounds=(1e-3, 1e3)) n_restarts_optimizer=10, max_iter_predict=100
K-nearest neighbors	n_neighbors=9, weights='uniform'

For unspecified model parameters, default values are used.

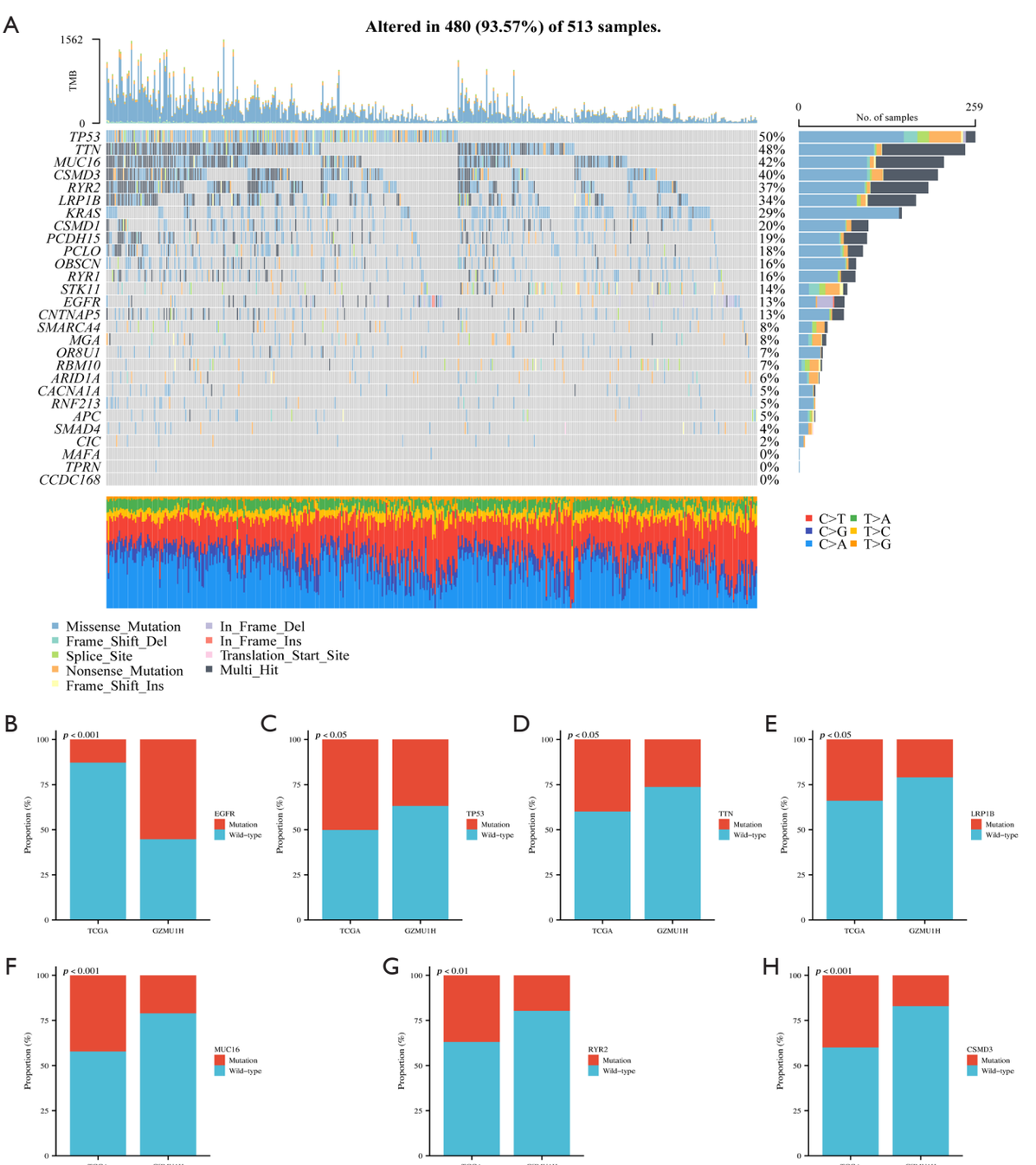

Figure S1 Mutation landscape of lung adenocarcinoma in the TCGA-LUAD cohort. Oncoplot demonstrating the highly mutant genes in the TCGA-LUAD dataset (A). Among the top ten mutated genes in the GZMU1H cohort, seven genes with significantly different mutant frequencies than the TCGA-LUAD cohort, including *EGFR* (B), *TP53* (C), *TTN* (D), *LRP1B* (E), *MUC16* (F), *RYR2* (G), and *CSMD3* (H), were found.

https://dx.doi.org/10.21037/tlcr-23-800

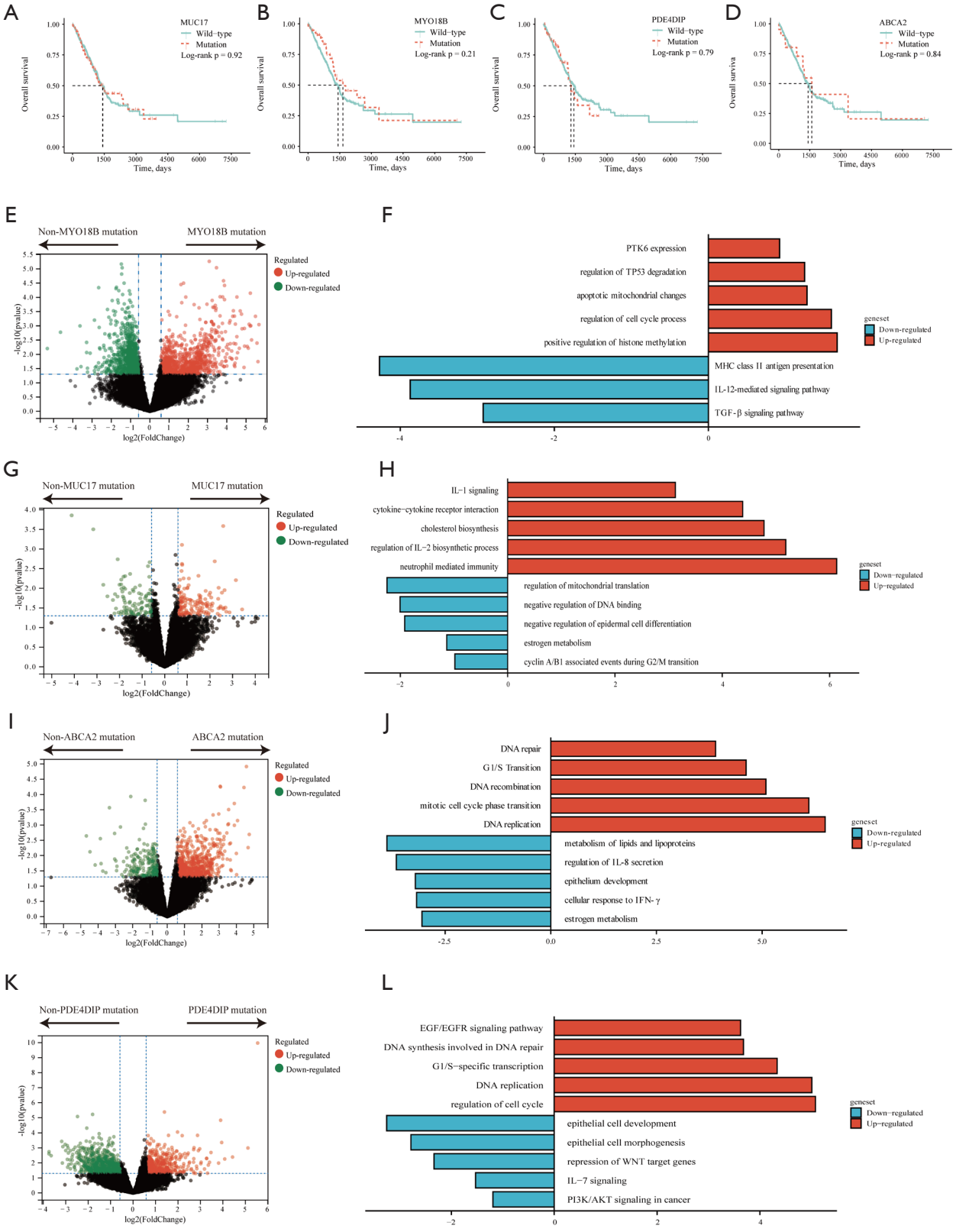

Figure S2 Transcriptomic spectrums and prognostic effects of specific gene mutations of early-stage non-squamous non-small cell lung cancer. Prognostic effects of monogenic mutation, including *MUC17* (A), *MYO18B* (B), *PDE4DIP* (C), and *ABCA2* (D), in the TCGA-LUAD cohort. Differentially expressed genes and corresponding enriched pathways of mutant versus wild-type *MYO18B* (E,F), *MUC17* (G,H), *ABCA2* (I,J), *PDE4DIP* (K,L) in the *GZMU1H* cohort. Red and green dots refer to significantly up-regulated and down-regulated genes, respectively. Black dots represent genes with insignificant changes in expression levels.

https://dx.doi.org/10.21037/tlcr-23-800

Table S4 Differentially expressed genes between tumor nest and paratumor tissues

A2M, ABCC4, ACKR1, ACKR2, ACKR3, ACKR4, ACO1, ACTG1, ACVR1B, ACVR2A, ACVR2B, ACVRL1, ADA2, ADAR, ADCYAP1R1, ADIPOR1, ADIPOR2, ADM2, ADRB1, ADRB2, ADRM1, AEN, AGER, AGRP, AGT, AGTR1, AGTR2, AHNAK, AKT2, AKT3, AMELX, AMHR2, ANGPT1, ANGPT4, ANGPTL1, ANGPTL3, ANGPTL4, ANGPTL5, ANGPTL6, ANGPTL7, ANOS1, ANXA6, AP3B1, APLN, APOBEC3A, APOH, APOM, AQP9, AR, ARG2, ARRB1, ARTN, AVPR1B, AVPR2, AZGP1, BACH2, BCL10, BCL3, BDNF, BECN1, BID, BIRC5, BLNK, BMP1, BMP2, BMP3, BMP5, BMP6, BMP8A, BMP8B, BMPR1A, BMPR2, BPHL, BPIFA1, BPIFA2, BPIFB2, BPIFB4, BRAF, BRD8, BST2, BTK, C5AR1, CACYBP, CALCRL, CALR, CAMP, CANX, CARD11, CASP3, CAT, CBL, CBLB, CBLC, CCK, CCL13, CCL14, CCL15, CCL16, CCL17, CCL18, CCL19, CCL20, CCL22, CCL23, CCL24, CCL25, CCL26, CCL28, CCL3, CCL3L1, CCL4, CCL5, CCL7, CCL8, CCR1, CCR10, CCR4, CCR5, CCR6, CCR7, CCR8, CCR9, CCRL2, CD14, CD19, CD1A, CD1B, CD1E, CD209, CD22, CD244, CD247, CD320, CD3D, CD3E, CD4, CD40LG, CD70, CD74, CD79A, CD79B, CD86, CDC42, CDH1, CDK4, CETP, CGB5, CHGB, CHUK, CIITA, CKLF, CLDN4, CLEC11A, CLEC4M, CMA1, CMKLR1, CMTM2, CMTM3, CMTM5, CMTM6, CMTM8, CNTF, CNTFR, COLEC10, COLEC12, CR2, CRABP1, CRABP2, CREB1, CRH, CRHR1, CRIM1, CRLF1, CRLF3, CSF2, CSF2RB, CSF3, CSF3R, CSH2, CSK, CSPG5, CSRP1, CST4, CTLA4, CTSB, CTSE, CTSG, CX3CL1, CX3CR1, CXCL1, CXCL10, CXCL11, CXCL12, CXCL13, CXCL14, CXCL16, CXCL17, CXCL2, CXCL3, CXCL5, CXCL6, CXCL8, CXCL9, CXCR1, CXCR2, CXCR3, CXCR4, CXCR5, CXCR6, CYBB, CYLD, CYSLTR2, DAXX, DCK, DDX17, DDX58, DEFA1, DEFA3, DEFB1, DEFB124, DEFB125, DEFB126, DEFB127, DEFB4A, DES, DKK1, DLL4, DUOX1, DUOX2, EBI3, ECD, EDN1, EDN2, EDN3, EDNRA, EDNRB, EGF, EGFR, EIF2AK2, ELAVL1, ELN, ENDOU, ENG, EPGN, EPO, EPOR, EPPIN, ERAP2, EREG, ESM1, ESR1, ESR2, ESRRA, ESRRB, F2R, F2RL1, FABP12, FABP4, FABP5, FABP7, FAM3B, FAM3C, FAM3D, FAS, FASLG, FCER1G, FCGR3A, FCGR3B, FCGRT, FGA, FGF1, FGF10, FGF11, FGF12, FGF13, FGF14, FGF17, FGF18, FGF19, FGF2, FGF21, FGF22, FGF23, FGF7, FGF7P6, FGF9, FGFR1, FGFR2, FGFR4, FGFRL1, FGR, FLT1, FLT3, FLT3LG, FLT4, FOS, FPR1, FPR2, FSHR, FURIN, FYN, GAL, GALR2, GCGR, GDF10, GDF11, GDF15, GDF3, GDF5, GDF6, GDF7, GDNF, GFAP, GHR, GHRHR, GHRL, GIPR, GLP2R, GMFB, GMFG, GNAI1, GNLY, GNRH1, GNRH2, GNRHR, GPER1, GPHA2, GPI, GPR17, GRAP2, GRB2, GREM1, GREM2, GRK2, GSK3B, GUCA2A, GZMB, HAMP, HBEGF, HCK, HDAC1, HDGF, HDGFL3, HFE, HGF, HMGB1, HNF4A, HNF4G, HRAS, HRG, HSP90AA1, HSP90AB1, HSPA1A, HSPA1B, HSPA1L, HSPA2, HSPA4, HSPA5, HSPA6, HSPA8, HTR3A, HTR3B, HTR3C, ICAM1, ICAM2, IDO1, IFITM1, IFNA1, IFNA13, IFNA21, IFNA5, IFNAR2, IFNB1, IFNE, IFNGR1, IFNGR2, IFNK, IFNL1, IFNL3, IGF1, IGF1R, IGHA1, IGHA2, IGHD, IGHE, IGHG1, IGHG2, IGHG3, IGHG4, IGHM, IGKC, IGLC1, IGLC2, IGLC3, IGLC6, IGLC7, IKBKB, IKBKE, IL10RA, IL10RB, IL11, IL11RA, IL12A, IL12B, IL12RB1, IL13, IL13RA2, IL15, IL15RA, IL16, IL17D, IL17RA, IL17RC, IL17RD, IL17RE, IL18, IL18R1, IL18RAP, IL1A, IL1B, IL1R1, IL1RL1, IL1RL2, IL2, IL20RA, IL20RB, IL21, IL21R, IL22RA2, IL23A, IL23R, IL27, IL27RA, IL2RA, IL31RA, IL33, IL34, IL36A, IL36G, IL36RN, IL37, IL3RA, IL4R, IL5, IL5RA, IL6, IL6ST, IL7R, ILK, INHBA, INHBB, INPP5D, INSL3, IREB2, IRF1, IRF3, IRF5, IRF7, ISG15, ISG20, ISG20L2, ITGAL, ITGAV, ITK, JAG1, JAK1, JAK2, JUN, JUND, KDR, KIR2DL1, KIR2DL3, KIR2DS4, KIR3DL1, KIR3DL2, KITLG, KL, KLKB1, KLRC1, KLRC2, KLRC3, KLRC4, KLRD1, KLRK1, LANCL1, LAT, LBP, LCN10, LCN12, LCN2, LCN6, LCNL1, LCP2, LEAP2, LEFTY2, LEPR, LGMN, LGR4, LGR5, LHCGR, LIF, LIFR, LILRB3, LMBR1, LMBR1L, LPA, LRP1, LRSAM1, LTA, LTB, LTB4R, LTB4R2, LTBP2, LTBP4, LTF, LYN, LYZ, MALT1, MANF, MAP2K1, MAP2K2, MAP3K14, MAP3K8, MAPK1, MAPK3, MAPK8, MAPT, MARCO, MASP1, MASP2, MAVS, MBL2, MC1R, MC2R, MC4R, MDK, MET, MIA, MICA, MIF, MMP12, MMP9, MPL, MPO, MSR1, MSTN, MTNR1A, MUC4, MUC5AC, MX1, MX2, MYDGF, NCK1, NCK2, NCR1, NCR2, NDP, NEDD4, NENF, NEO1, NFAT5, NFATC1, NFATC2, NFATC3, NFKBIA, NFKBIB, NFKBIE, NFKBIZ, NFYB, NGF, NLRX1, NMB, NMBR, NOD1, NOD2, NODAL, NOS1, NOS2, NOX1, NOX4, NPFF, NPPA, NPPC, NPR1, NPR3, NR1D1, NR1D2, NR1H2, NR1H3, NR1I3, NR2C1, NR2C2, NR2E1, NR2E3, NR2F1, NR2F2, NR2F6, NR3C1, NR3C2, NR4A1, NR4A2, NR4A3, NR5A2, NR6A1, NRG1, NRG2, NRG3, NRG4, NRP1, NRP2, NRTN, NTF3, NUDT6, OAS1, OASL, OBP2A, OGFR, OGN, OLR1, OPRD1, OPRK1, OPRL1, ORM1, ORM2, OSGIN1, OSM, OSMR, OSTN, OXT, OXTR, PAEP, PAK1, PAK2, PAK4, PAK6, PDF, PDGFA, PDGFB, PDGFC, PDGFD, PDGFRA, PDGFRB, PDGFRL, PDIA3, PDK1, PF4, PGC, PGF, PGLYRP1, PGLYRP2, PGLYRP3, PGLYRP4, PGR, PI15, PI3, PIK3CA, PIK3CB, PIK3CG, PIK3R1, PIK3R2, PIK3R5, PLA2G2A, PLAU, PLAUR, PLCG1, PLCG2, PLSCR1, PLTP, PLXNA2, PLXNA3, PLXNA4, PLXNB1, PLXNB2, PLXNB3, PLXNC1, PLXND1, PMCH, PML, PNOC, PPARG, PPBP, PPBPP2, PPIA, PPP3CA, PPP3CB, PPP3CC, PPP3R2, PPP4C, PRDX1, PRDX2, PRF1, PRKCA, PRKCB, PRKCG, PRKCQ, PROC, PROK2, PSMB8, PSMC1, PSMC2, PSMC3, PSMC4, PSMD1, PSMD10, PSMD11, PSMD13, PSMD14, PSMD2, PSMD3, PSMD4, PSMD6, PSMD7, PSMD8, PSME1, PSME2, PSME3, PSPN, PTAFR, PTGDR, PTGDR2, PTGDS, PTGER2, PTGER3, PTGER4, PTGFR, PTH1R, PTHLH, PTK2B, PTN, PTPN11, PTPN6, PTPRC, PTX3, QRFP, RABEP1, RABEP2, RAC1, RAC3, RAET1E, RAET1L, RAF1, RARA, RARB, RASGRP3, RBP1, RBP2, RBP4, RBP5, REG1A, RELB, RETN, RFX5, RFXANK, RFXAP, RHOA, RLN2, RLN3, RNASE2, RNASE7, RNASEL, ROBO1, ROBO2, ROBO3, RORA, RORC, RSAD2, RXFP1, RXFP2, RXRA, RXRB, RXRG, S100A1, S100A10, S100A11, S100A13, S100A14, S100A16, S100A2, S100A3, S100A6, S100A7, S100A9, S100B, S100P, S100Z, S1PR1, S1PR2, SAA1, SAA2, SBDS, SCGB3A1, SDC1, SDC2, SDC3, SDC4, SECTM1, SEMA3B, SEMA3D, SEMA3E, SEMA3F, SEMA3G, SEMA4B, SEMA4C, SEMA4F, SEMA4G, SEMA5A, SEMA6A, SEMA6C, SEMA6D, SEMA7A, SERPIND1, SFTPA1, SFTPA2, SFTPD, SH2D1A, SH2D1B, SH3BP2, SHC1, SHC2, SHC3, SKIV2L, SLC11A1, SLC40A1, SLIT2, SLPI, SOCS1, SOD1, SORT1, SOS1, SOS2, SP1, SPINK5, SPP1, SST, SSTR1, SSTR5, STAB2, STAT1, STAT3, SYTL1, TACR1, TANK, TAP1, TAP2, TAPBP, TBK1, TCF7L2, TEC, TEK, TFR2, TFRC, TGFA, TGFB2, TGFBR2, TGFBR3, THRA, THRB, TIE1, TINAGL1, TK2, TKFC, TLR1, TLR3, TLR4, TLR8, TMPRSS6, TMSB10, TMSB15A, TMSB15B, TMSB4X, TMSB4XP8, TNC, TNFAIP3, TNFRSF10A, TNFRSF10B, TNFRSF10C, TNFRSF10D, TNFRSF11A, TNFRSF12A, TNFRSF13B, TNFRSF13C, TNFRSF14, TNFRSF17, TNFRSF18, TNFRSF19, TNFRSF1B, TNFRSF21, TNFRSF4, TNFRSF6B, TNFRSF8, TNFRSF9, TNFSF11, TNFSF12, TNFSF13, TNFSF14, TNFSF15, TNFSF18, TNFSF4, TNFSF8, TNFSF9, TPM2, TRAF3, TRAV19, TRAV2, TRAV21, TRAV22, TRAV27, TRAV29DV5, TRAV3, TRAV4, TRAV5, TRBV19, TRBV27, TRBV28, TRBV30, TRBV9, TRDC, TRDV3, TRGC1, TRGC2, TRGV2, TRGV3, TRGV4, TRGV5, TRGV8, TRGV9, TRH, TRHR, TRIM22, TRIM27, TRPC4AP, TSHB, TSLP, TUBB3, TXK, TXLNA, TYK2, TYMP, TYROBP, UBR1, UCN, UCN2, UCN3, ULBP2, ULBP3, UMODL1, UNC93B1, UTS2B, VAV2, VAV3, VCAM1, VDR, VEGFA, VEGFB, VEGFC, VEGFD, VGF, VIM, VIP, VIPR1, WFDC2, WFIKKN1, WNT5A, XCL1, XCL2, XCR1, ZAP70, ZC3HAV1, ZC3HAV1L, ZYX

https://dx.doi.org/10.21037/tlcr-23-800

Table S5 Gene expression levels with prognostic significance in the univariate Cox regression analysis

Gene	P value	HR	95% CI_L	95% CI_U
CCR9	0.017	3.28E-05	6.65E-09	0.162
KLRC4	0.023	1.66E-04	8.95E-08	0.309
KIR2DL3	0.050	0.004	1.69E-05	0.996
KLRC1	0.050	0.007	5.36E-05	0.997
KLRD1	0.004	0.009	3.46E-04	0.218
NCR1	0.016	0.009	2.06E-04	0.413
IL27	0.033	0.017	4.26E-04	0.718
TXK	0.023	0.130	0.022	0.758
PTGDR	0.040	0.137	0.021	0.915
CD244	0.025	0.160	0.032	0.793
IL18RAP	0.044	0.196	0.040	0.960
DUOX2	0.013	0.241	0.078	0.745
IL18R1	0.029	0.251	0.073	0.866
LCN10	0.049	0.266	0.071	0.995
CXCR6	0.007	0.266	0.102	0.698
KLRK1	0.018	0.290	0.105	0.805
GPR17	0.044	0.310	0.099	0.970
PPP3CC	0.045	0.318	0.104	0.974
HDGFL3	0.047	0.347	0.123	0.984
PLCG2	0.009	0.366	0.172	0.778
TRAV3	0.045	0.379	0.147	0.979
IL34	0.049	0.396	0.158	0.995
SEMA6A	0.042	0.415	0.178	0.969
GIPR	0.032	0.421	0.191	0.928
ICAM2	0.024	0.438	0.214	0.896
PTK2B	0.003	0.442	0.257	0.758
JAK2	0.035	0.447	0.211	0.944
BMP6	0.012	0.461	0.253	0.841
TRIM22	0.007	0.475	0.276	0.819
S1PR1	0.029	0.492	0.260	0.930
EPOR	0.047	0.494	0.246	0.991
VIPR1	0.042	0.526	0.283	0.977
ADRB2	0.030	0.624	0.408	0.955
PI3	0.030	0.637	0.424	0.957
INHBB	0.026	0.679	0.482	0.956
DUOX1	0.027	0.708	0.522	0.961
CD79A	0.028	0.724	0.542	0.966
IGHG3	0.041	0.805	0.655	0.991
PLAU	0.031	1.310	1.020	1.670
SPP1	0.005	1.347	1.090	1.660
TUBB3	0.050	1.381	1.000	1.910
HTR3A	0.046	1.453	1.010	2.100
CRABP2	0.001	1.532	1.190	1.970
PLXNB3	0.040	1.542	1.020	2.330
F2RL1	0.027	1.585	1.050	2.380
PPIA	0.035	1.609	1.030	2.500
IL13RA2	0.015	1.621	1.100	2.390
EGFR	0.028	1.643	1.060	2.560
PLAUR	0.017	1.663	1.090	2.530
PGLYRP4	0.043	1.715	1.020	2.890
ULBP2	0.008	1.747	1.160	2.640
LGR4	0.006	1.880	1.190	2.960
IL31RA	0.003	2.062	1.290	3.310
IL11	0.002	2.163	1.330	3.510
PSMD4	0.041	2.207	1.030	4.720
GDF5	0.016	2.486	1.180	5.230
NGF	0.038	3.060	1.060	8.800
CCR8	0.034	3.826	1.100	13.300
HFE	0.044	3.925	1.040	14.800
EPGN	0.038	4.016	1.080	14.900
IL1A	0.008	4.366	1.470	13.000
CRHR1	0.022	100.150	1.940	5.17E+03
HTR3B	0.044	1.03E+03	1.190	8.97E+05
PPBPP2	0.002	2.32E+04	39.500	1.36E+07
MBL2	0.010	1.42E+05	17.500	1.16E+09

HR, hazard ratio; CI_L, lower bounds of the 95% confidence interval; CI_U, upper bounds of the 95% confidence interval.

https://dx.doi.org/10.21037/tlcr-23-800

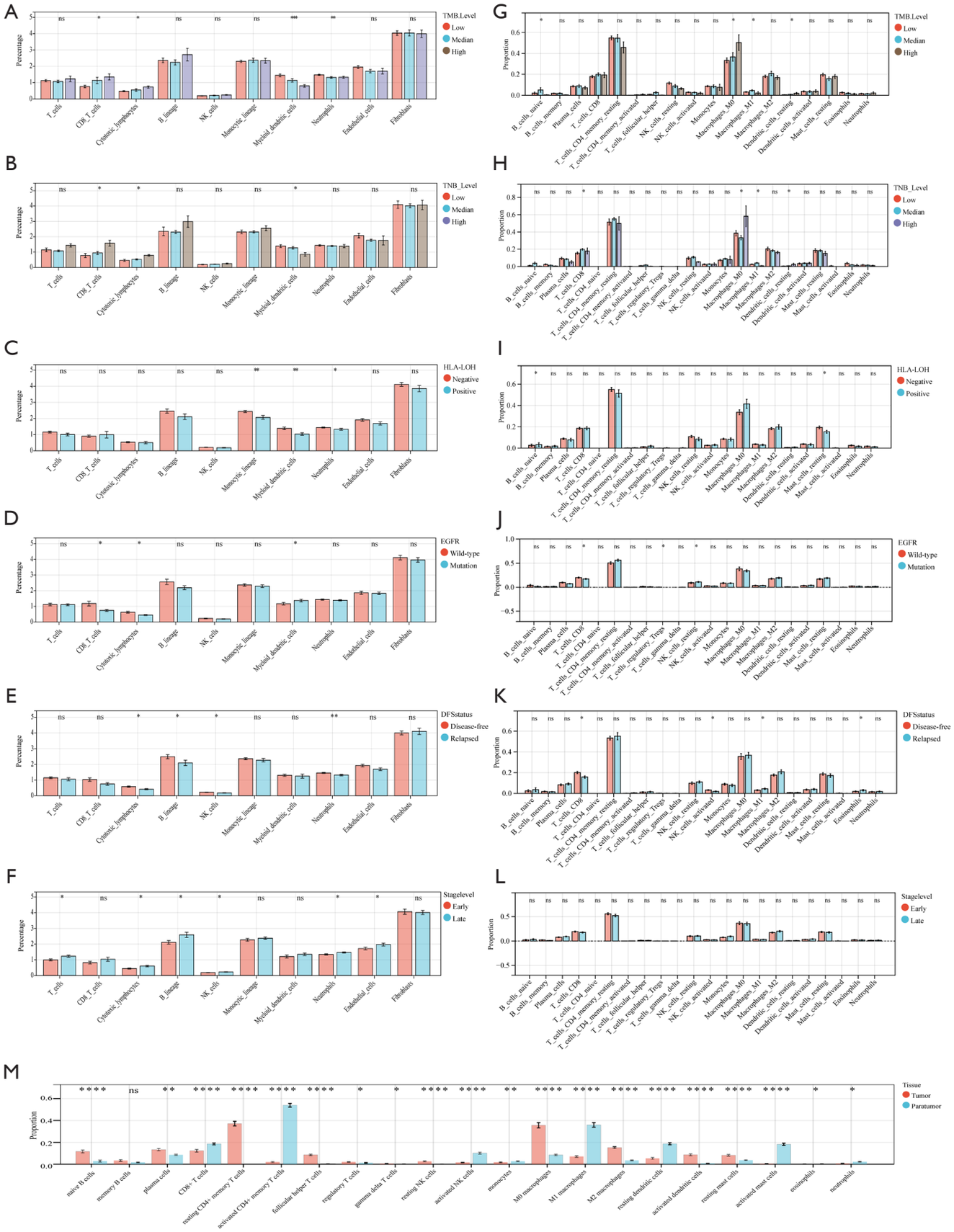

Figure S3 Immune infiltration differences between tumor nest and adjacent tissues. Intratumoral immune infiltration differences between different tumor mutational burden (TMB) levels (A), tumor neoantigen burden (TNB) levels (B), human leukocyte antigen loss of heterozygosity (HLA-LOH) status (C), EGFR mutation status (D), disease-free survival (DFS) status (E), and cTNM stage level (F), as evaluated by the MCP-counter algorithm. Intrastromal immune infiltration differences between different TMB levels (G), TNB levels (H), HLA-LOH status (I), EGFR mutation status (J), DFS status (K), and cTNM stage level (L), as evaluated by the CIBERSORT algorithm. Comparison of immune infiltration difference between tumor nest and paratumor tissue (M). Comparison of continuous data by Kruskal-Wallis test. *, P<0.05; **, P<0.01; ****, P<0.0001; ns, non-significant.

https://dx.doi.org/10.21037/tlcr-23-800

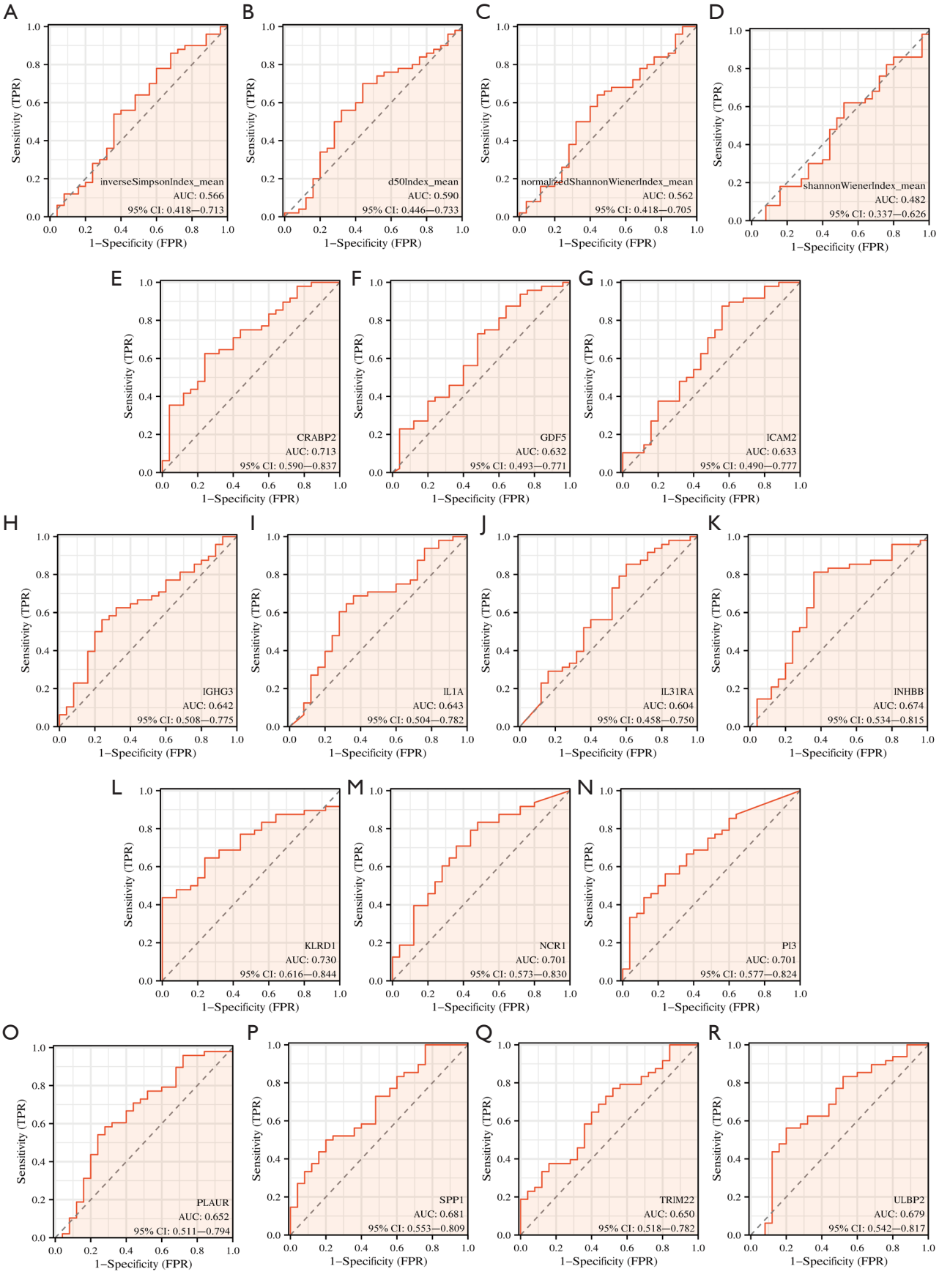

Figure S4 The predictive accuracy of single omics/biomarker in disease-free survival. T cell receptor repertoire diversity features (A-D), and transcriptomic characteristics (E-R) showed limited performance in predicting prognosis.

https://dx.doi.org/10.21037/tlcr-23-800

Table S6 Performance of the machine learning algorithms in the training cohort

	Accuracy	Precision	Recall	F1-score	AUC
Clinical + RNA					
SVM	0.833	0.813	0.650	0.722	0.818
DTC	0.933	0.900	0.900	0.900	0.978
ETC	1.000	1.000	1.000	1.000	1.000
GBC	0.950	1.000	0.850	0.919	0.998
GPC	0.975	0.975	0.975	0.975	0.999
KNN	0.767	0.800	0.400	0.533	0.815
RF	0.983	1.000	0.950	0.974	0.975
Clinical +DNA+RNA+TCR					
SVM	0.733	0.625	0.500	0.556	0.735
DTC	0.917	0.857	0.900	0.878	0.973
ETC	1.000	1.000	1.000	1.000	1.000
GBC	0.667	0	0	0	0.986
GPC	0.813	0.931	0.675	0.783	0.904
KNN	0.800	0.833	0.500	0.625	0.869
RF	0.933	1.000	0.800	0.889	1.000
Clinical + DNA					
SVM	0.767	0.750	0.450	0.563	0.829
DTC	0.983	1.000	0.950	0.974	0.999
ETC	0.900	1.000	0.700	0.824	0.988
GBC	1.000	1.000	1.000	1.000	1.000
GPC	0.975	0.975	0.975	0.975	0.997
KNN	0.783	0.733	0.550	0.629	0.803
RF	0.833	0.917	0.550	0.687	0.936
Clinical + TCR					
SVM	0.717	0.600	0.450	0.514	0.685
DTC	0.917	0.941	0.800	0.865	0.968
ETC	1.000	1.000	1.000	1.000	1.000
GBC	1.000	1.000	1.000	1.000	1.000
GPC	0.875	0.917	0.825	0.868	0.890
KNN	0.767	0.800	0.400	0.533	0.804
RF	0.817	0.846	0.550	0.667	0.926
DNA+RNA					
SVM	0.783	0.733	0.550	0.629	0.860
DTC	0.933	0.833	1.000	0.909	0.972
ETC	0.917	1.000	0.750	0.857	0.992
GBC	0.667	0	0	0	0.973
GPC	1.000	1.000	1.000	1.000	1.000
KNN	0.733	0.667	0.400	0.500	0.819
RF	0.983	1.000	0.950	0.974	1.000
DNA+RNA+TCR					
SVM	0.650	0.455	0.250	0.323	0.695
DTC	0.967	0.950	0.950	0.950	0.997
ETC	0.983	1.000	0.950	0.974	1.000
GBC	1.000	1.000	1.000	1.000	1.000
GPC	0.788	0.829	0.725	0.773	0.869
KNN	0.800	0.900	0.450	0.600	0.850
RF	0.967	1.000	0.900	0.947	1.000

SVM, support vector machine; DTC, decision tree classifier; ETC, extra tree classifier; GBC, gradient boosting classifier; GPC, Gaussian process classifier; KNN, K-nearest neighbors; RF, random forest.

https://dx.doi.org/10.21037/tlcr-23-800

Table S7 Performance of the machine learning algorithms in the testing cohort

	Accuracy	Precision	Recall	F1-score	AUC
Clinical + RNA					
DTC	0.688	0.600	0.500	0.545	0.692
ETC	0.875	1.000	0.667	0.800	0.933
GBC	0.688	1.000	0.167	0.286	0.800
GPC	0.688	1.000	0.167	0.286	0.733
KNN	0.750	1.000	0.333	0.500	0.867
RF	0.813	1.000	0.500	0.667	0.833
SVM	0.813	1.000	0.500	0.667	0.900
Clinical +DNA+RNA+TCR					
DTC	0.625	0.500	0.333	0.400	0.667
ETC	0.688	0.667	0.333	0.444	0.833
GBC	0.625	0	0	0	0.717
GPC	0.750	0.625	0.833	0.714	0.817
KNN	0.625	0	0	0	0.933
RF	0.625	0	0	0	0.817
SVM	0.563	0.400	0.333	0.364	0.617
Clinical + DNA					
DTC	0.625	0.500	0.333	0.400	0.567
ETC	0.625	0.500	0.167	0.250	0.717
GBC	0.625	0.500	0.333	0.400	0.433
GPC	0.563	0	0	0	0.517
KNN	0.875	0.833	0.833	0.833	0.767
RF	0.625	0	0	0	0.733
SVM	0.688	1.000	0.167	0.286	0.750
Clinical + TCR					
DTC	0.563	0.400	0.333	0.364	0.508
ETC	0.688	1.000	0.167	0.286	0.650
GBC	0.625	0	0	0	0.650
GPC	0.813	0.714	0.833	0.769	0.850
KNN	0.750	1.000	0.333	0.500	0.833
RF	0.688	1.000	0.167	0.286	0.600
SVM	0.625	0.500	0.167	0.250	0.450
DNA+RNA					
DTC	0.750	0.750	0.500	0.600	0.683
ETC	0.625	0.500	0.167	0.250	0.700
GBC	0.625	0	0	0	0.833
GPC	0.625	0.500	0.333	0.400	0.817
KNN	0.688	0.667	0.333	0.444	0.817
RF	0.688	1	0.167	0.286	0.767
SVM	0.625	0.500	0.167	0.250	0.667
DNA+RNA+TCR					
DTC	0.625	0.500	0.167	0.250	0.608
ETC	0.625	0.500	0.167	0.250	0.683
GBC	0.688	1.000	0.167	0.286	0.633
GPC	0.875	0.833	0.833	0.833	0.900
KNN	0.625	0	0	0	0.758
RF	0.625	0	0	0	0.683
SVM	0.563	0	0	0	0.483

DTC, decision tree classifier; ETC, extra tree classifier; GBC, gradient boosting classifier; GPC, Gaussian process classifier; KNN, K-nearest neighbors; RF, random forest; SVM, support vector machine.

https://dx.doi.org/10.21037/tlcr-23-800